

Defect Passivation of 2D Semiconductors by Fixating Chemisorbed Oxygen Molecules via *h*-BN Encapsulations

*Jin-Woo Jung, Hyeon-Seo Choi, Young-Jun Lee, Youngjae Kim, Takashi Taniguchi, Kenji Watanabe, Min-Yeong Choi, Jae Hyuck Jang, Hee-Suk Chung, Dohun Kim, Youngwook Kim, and Chang-Hee Cho**

Jin-Woo Jung, Hyeon-Seo Choi, Young-Jun Lee, Dohun Kim, Youngwook Kim, Chang-Hee Cho

Department of Physics and Chemistry, Daegu Gyeongbuk Institute of Science and Technology (DGIST), Daegu 42988, South Korea

E-mail: chcho@dgist.ac.kr

Youngjae Kim

School of Physics, Korea Institute for Advanced Study (KIAS), Seoul 02455, South Korea

Takashi Taniguchi

International Center for Materials Nanoarchitectonics, National Institute for Materials Science, Tsukuba 305-0044, Japan

Kenji Watanabe

Research Center for Functional Materials, National Institute for Materials Science, Tsukuba 305-0044, Japan

Min-Yeong Choi, Jae Hyuck Jang, Hee-Suk Chung

Electron Microscopy and Spectroscopy Team, Korea Basic Science Institute, Daejeon 34133, South Korea

Jae Hyuck Jang

Graduate School of Analytic Science and Technology, Chungnam National University, Daejeon 34134, South Korea

Hexagonal boron nitride (*h*-BN) is a key ingredient for various two-dimensional (2D) van der Waals heterostructure devices, but the exact role of *h*-BN encapsulation in relation to the internal defects of 2D semiconductors remains unclear. Here, we report that *h*-BN encapsulation greatly removes the defect-related gap states by stabilizing the chemisorbed oxygen molecules onto the defects of monolayer WS₂ crystals. Electron energy loss spectroscopy (EELS) combined with theoretical analysis clearly confirms that the oxygen molecules are chemisorbed onto the defects of WS₂ crystals and are fixated by *h*-BN encapsulation, with excluding a possibility of oxygen molecules trapped in bubbles or wrinkles formed at the interface between WS₂ and *h*-BN. Optical spectroscopic studies show that *h*-BN encapsulation prevents the desorption of oxygen molecules over various excitation and ambient conditions, resulting in a greatly lowered and stabilized free electron density in monolayer WS₂ crystals. This suppresses the exciton annihilation processes by two orders of magnitude compared to that of bare WS₂. Furthermore, the valley polarization becomes robust against the various excitation and ambient conditions in the *h*-BN encapsulated WS₂ crystals.

1. Introduction

Monolayer transition metal dichalcogenides (TMDs) have emerged as a platform to examine various exciton species such as trions, biexcitons, interlayer excitons, and moiré excitons due to the strong inter-particle interactions.^[1-4] Furthermore, the valley-dependent optical selection rules given by the broken inversion symmetry enable the selective generation of excitons in the particular valley (+K or -K) using circularly polarized light,^[5] providing the opportunity for applications toward valleytronic devices. However, the external disorders in close proximity of monolayer TMDs such as substrate-induced surface roughness and adsorbates can significantly alter the excitonic properties of two-dimensional (2D) TMD materials, hindering the observation of the unique properties in monolayer TMDs.^[6,7]

In an attempt to reduce the disorder from substrates, it has been proposed to encapsulate TMD materials using hexagonal boron nitride (*h*-BN) layers.^[8,9] Recently, it has been shown that *h*-BN encapsulation enables to observe the intrinsic optical properties of monolayer TMDs, including the excitonic linewidth with homogeneous broadening limit^[9] and the suppression of exciton annihilation processes.^[10] As the origin, the reduced substrate disorders have often been suggested in the previous works,^[9,10] but the excitonic properties of TMDs on *h*-BN substrates show large discrepancies from those of TMDs encapsulated by *h*-BN.^[11,12] On the other hand, previous investigations have shown that the oxygen molecules on the surface of TMDs also alter the electronic and optical properties of 2D TMD materials.^[13-18] The adsorption of the

oxygen molecules occurs on the defects with relatively lower kinetic barrier rather than the perfect sites of TMD materials,^[18] and the oxygen molecules unlike other molecules can only be chemisorbed at chalcogen vacancies due to isovalent valence electrons (two unpaired electrons) with the chalcogen atom.^[14,15] This chemisorption of oxygen molecules at the defect sites removes the defect-related gap states without significantly altering the electronic band structures of TMD materials.^[13,14] Thus, the oxygen molecules, that are supplied during the exposure of TMDs into the atmosphere, can significantly change the properties of defect-related states through the chemical adsorption process. In this regard, *h*-BN encapsulation can play a crucial role in the defect states of TMDs, in which the *h*-BN layers fixate the adsorbed oxygen molecules on the TMD defects and facilitate the interaction between the oxygen molecules and the defect states. However, the role of *h*-BN encapsulation in relation to the defects of TMDs remains unexplored.

In this work, we found that *h*-BN encapsulation stabilizes the chemisorbed oxygen molecules on the defect sites of monolayer WS₂ crystals, which greatly passivates the defect-related gap states along with the decrease in the free electron density. Electron energy loss spectroscopy (EELS) combined with theoretical analysis clearly reveals that the oxygen molecules are chemisorbed onto the defects of WS₂ crystals and are fixated by *h*-BN encapsulation, that excludes a possibility of oxygen molecules trapped in bubbles or wrinkles formed at the interface between WS₂ and *h*-BN. Optical spectroscopic studies show that *h*-BN encapsulation prevents the desorption of oxygen molecules over various excitation and ambient conditions, resulting in a greatly lowered and stabilized free electron density in monolayer WS₂ crystals. This suppresses the exciton annihilation processes by two orders of magnitude compared to that of bare WS₂. Furthermore, due to the stabilized free electron density in the *h*-BN encapsulated WS₂ crystals, the valley polarization becomes robust against the elevated excitation condition.

2. Results and Discussion

Figure 1a shows a schematic illustration showing that the fixated oxygen molecules by the *h*-BN layers effectively passivate defects of the WS₂. We considered the chemisorption type, where the oxygen molecule chemically bonds to three surrounding tungsten atoms, which is the most common configuration for the oxygen chemisorption (inset image of Figure 1a) in the S-based TMDs.^[14-17] The chemisorbed oxygen molecules at the chalcogen vacancies can also be dissociated into two oxygen atoms, leading to a dissociative chemisorption, which occupies the sulfur vacancies with the dissociated oxygen atoms.^[13-15] However, in the case of the WS₂ used

in our study, the kinetic barrier for the O₂-chemisorption (0.56 eV) is lower than that for the O₂-dissociative chemisorption process (0.76 eV). It is estimated that the probability of the O₂-chemisorption is 1000 times higher than that of the dissociative chemisorption (see Figure S1 in Supporting Information). Thus, the oxygen chemisorption on the monolayer WS₂ crystals would have the final configuration of the O₂-chemisorption rather than the O₂-dissociative chemisorption.^[14] The major molecules such as N₂, O₂, and H₂O in air can be weakly physisorbed at both the pristine surface and defect sites of WS₂. However, this physisorption has virtually no influence on the electronic and optical properties of the WS₂ monolayer due to easy desorption of physisorbed molecules.^[14] In addition, our first-principle calculations demonstrate that the oxygen molecules can only be chemisorbed onto the defects (sulfur vacancy) and attain a fully stable chemisorption state, indicating that the oxygen molecules can be majorly adsorbed onto the WS₂ in the air. The detailed theoretical calculation results on molecular interactions with the sulfur vacancy and pristine surface of WS₂ are provided in Supporting Information S2 and S3. To investigate the role of oxygen fixation in the excitonic properties of monolayer WS₂ with excluding the effects of disorders induced by the substrates, we studied *h*-BN encapsulated WS₂ crystals suspended on line trenches with a linewidth of 1.8 μm in comparison with bare WS₂, as shown in Figures 1b,d. Scanning electron microscope images confirm the suspended structures for both the bare (Figure 1b) and *h*-BN encapsulated (Figure 1d) WS₂ crystals on the line trenches (see Figure S4 in Supporting Information). The monolayered WS₂ crystals used in this study were grown on sapphire substrates using a chemical vapor deposition (CVD) method.^[19] Mechanically exfoliated *h*-BN flakes with a thickness of ~40 nm were used as the encapsulating layers in the *h*-BN/WS₂/*h*-BN structures. The detailed sample preparation processes are described in the methods. Figures 1c,e display the spatial photoluminescence profiles of the bare (Figure 1c) and *h*-BN encapsulated (Figure 1e) WS₂ suspended on the line trenches, respectively. The steady-state photoluminescence measurements were carried out at a low level of excitation (~0.065 kW/cm²) to rule out the heating effect. It is worth noting that the photoluminescence intensity becomes stronger in the suspended regions than in the supported regions for both the bare and *h*-BN encapsulated WS₂ crystals due to the enhanced local field effect by optical interference in the trench region.^[7] To confirm the exciton species, the photoluminescence spectra were measured at a cryogenic temperature of 77 K under a vacuum level of ~1 × 10⁻⁵ Torr, as shown in Figure 1f. For the *h*-BN encapsulated WS₂, the neutral exciton (X⁰) and the trion (X⁻) are identified at energies of 2.042 and 2.001 eV, respectively, while the bare WS₂ shows three species of the neutral exciton (X⁰), trion (X⁻), and defect-related trapped exciton (L) at 2.087, 2.042, and 2.026 eV,

respectively. The energy of neutral exciton was assigned by measuring the differential reflectance spectra (see Figure S5 in Supporting Information), and those of trion and defect-related trapped exciton were identified by the energy differences from the neutral exciton.^[20,21] Compared to the bare WS₂ showing the emission prevailed by the trion and the defect-related trapped exciton, the *h*-BN encapsulated WS₂ exhibits the predominant emission from the neutral exciton with homogeneous linewidth of the 6 meV,^[9] indicating that the defect-induced free electrons and inhomogeneous broadening are substantially reduced by the encapsulating WS₂ with *h*-BN layers. These results indicate that the oxygen fixation by *h*-BN encapsulation can play a crucial role in the defect removal with reducing the free electron density. To directly confirm the fixation effect of the adsorbed oxygen molecules on the defects, the change in excitonic spectra was monitored under the different ambient conditions of air and vacuum, as shown in Figure 1g (see Figure S6 in Supporting Information). Striking features are observed for the bare WS₂ crystals, showing that the spectral weight of neutral excitons is predominant over that of trions under ambient air condition, whereas that of trions becomes larger than that of neutral excitons under vacuum. These results indicate that the oxygen adsorbates on the defect sites are released by changing the ambient condition from air to vacuum, raising the density of free electrons in the bare WS₂ crystals under vacuum.^[16,17] As shown in Figures S7, the *h*-BN encapsulated WS₂ samples fabricated under an inert (N₂) environment exhibit much stronger trion intensity (higher free electron concentration) compared to that of the *h*-BN encapsulated WS₂ fabricated in the air. The spectral feature is very similar to that of the bare WS₂ measured in the vacuum environment (see top panels in Figures 1f and 1g). Furthermore, the exfoliated monolayer WS₂ and WSe₂ with a lower density of chalcogen vacancies give rise to a less change in the free electron density against the variation of the ambient conditions, implying that the oxygen molecules are mostly adsorbed on the chalcogen vacancies (see Figure S8 in Supporting Information). In contrast, the *h*-BN encapsulated WS₂ crystals exhibit almost the same spectra prevailed by the neutral excitons regardless of the ambient conditions, highlighting that the *h*-BN encapsulation effectively removes the internal defects by stabilizing the oxygen molecules adsorbed onto WS₂ crystals.

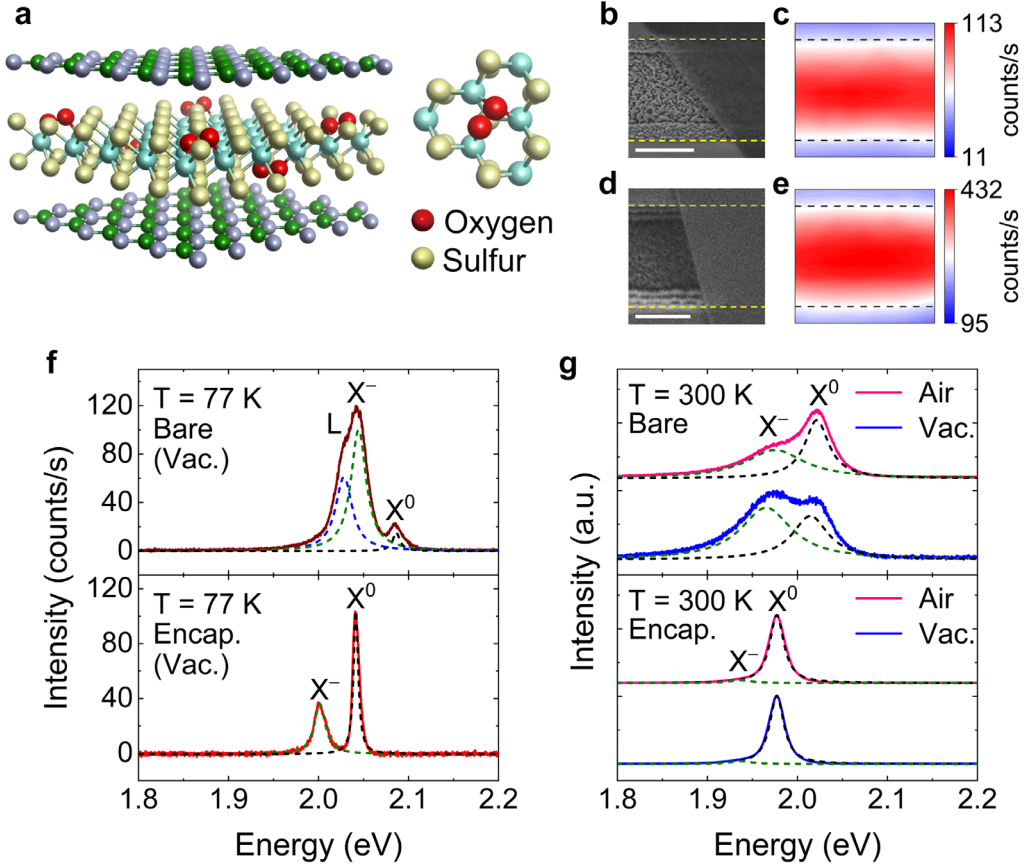


Figure 1. a) Schematic illustration showing the chemisorbed oxygen molecules anchored by the *h*-BN encapsulation. Right inset image represents the detailed atomic configuration of the chemisorbed oxygen molecule at the sulfur vacancy. b) Scanning electron microscope image of the bare WS₂ crystals on the line trenches. c) Spatial photoluminescence profile measured from the bare WS₂ on the line trench. d) Scanning electron microscope image of the *h*-BN encapsulated WS₂ crystals on the line trench. e) Spatial photoluminescence profile measured from the *h*-BN encapsulated WS₂ on the line trenches. The yellow and black dashed lines marked in (b,d) and (c,e) indicate the boundary of the suspended and supported regions. The scale bars of (b,d) are 1 μm . f) Photoluminescence spectra for the bare (top panel) and *h*-BN encapsulated (bottom panel) WS₂ measured at a cryogenic temperature of 77 K under a vacuum level of $\sim 1 \times 10^{-5}$ Torr. g) Photoluminescence spectra for the bare (top panel) and *h*-BN encapsulated (bottom panel) WS₂ measured under different ambient conditions of air and vacuum ($T = 300$ K). Each photoluminescence spectrum was fitted by Lorentzian functions. The black, olive, and blue dashed lines represent the neutral exciton (X^0), trion (X^-), and defect-related trapped exciton (L) states, respectively.

The EELS analysis for oxygen K -edge confirms that the h -BN encapsulation anchors the chemisorbed oxygen molecules onto the defects of monolayer WS_2 crystals. Figure 2a displays the EELS spectra of the oxygen K -edge for the h -BN encapsulated WS_2 , bare WS_2 , and h -BN flake crystals. The h -BN encapsulated WS_2 crystals show the oxygen K -edge peaks centered at 538 and 556 eV, whereas any oxygen-related features are not observed for the bare WS_2 and the h -BN crystals. This suggests that the adsorbed oxygen molecules on WS_2 are fixated by the h -BN encapsulation (see Figure S9 in Supporting Information). Figures 2b-e show the EELS maps for the boron (b), nitrogen (c), oxygen (d) K -edge, and the sulfur (e) L -edge measured from the h -BN encapsulated WS_2 . Note that the elemental signal displayed for a pixel in the EELS map is the sum of the elemental signals detected through 2D scanning using an electron beam with a spatial resolution of 1 Å over an area of 20 nm \times 20 nm. The spatial EELS maps confirm that the oxygen K -edge signal is markedly weak compared to those of other elements, and is randomly distributed in the 2D plane of h -BN encapsulated WS_2 samples. This strongly indicates that the oxygen molecules are chemisorbed on the randomly distributed local defects in WS_2 crystals (see Figure S10 in Supporting Information).

To discover the adsorption types of the adsorbed oxygen molecules by h -BN encapsulation, we demonstrate the theoretical EELS spectra of oxygen K -edge for the physisorbed oxygen molecule on the pristine WS_2 (Figure 2f) and chemisorbed oxygen molecule at the sulfur vacancy site of the WS_2 (Figure 2g). To understand the underlying physics for the EELS results, we performed theoretical EELS calculations based on the first-principles calculations implemented in the full-potential linearized plane wave (FLAPW) + local orbitals with the ELK code. Here, we used the pseudo core-hole method, where the self-consistent calculation is made in terms of one of the oxygen nuclei constrained to be positively charged (+1e) and an additional electron (-1e) is simultaneously constrained to occupy the conduction orbitals. After the self-consistent calculation, the Kohn-Sham orbitals become well defined, and then we compute the photon-absorption matrix elements between the core orbital (s -orbital) of the oxygen nuclei and the unoccupied conduction bands, which corresponds to the dielectric function for EELS spectra (see Supporting Information S11 for more detail).

The calculated EELS spectrum for the physisorbed oxygen molecule on the pristine WS_2 indicates the two main peaks at 530 eV and 539 eV, which originate from the transition of the core electrons to two kinds of trivial hybridized states in the oxygen molecule, featured as anti-bonding orbital π^* (top) and σ^* (bottom) distributions, respectively (see the inset of Figure 2f), whereas the calculated oxygen K -edge peaks for the chemisorbed oxygen molecule appear at the energy loss positions of 538 and 555 eV (labelled as A and B on the spectrum), respectively.

Since the core-hole excitation makes the oxygen molecule to have an asymmetric potential, the π^* orbital distribution in the inset reflects asymmetric densities. As shown in Figure 2g, the calculated EELS spectrum (red dashed) for a chemisorbed oxygen molecule is in good agreement with that of the *h*-BN encapsulated WS₂ (blue line), indicating that the fixated oxygen molecules by the *h*-BN encapsulation are chemisorbed at the defect sites of the WS₂. The anti-bonding orbital π^* peak (530 eV) is absent for the chemisorbed oxygen molecule in the calculated EELS spectrum. The disappearance of π -bonding is commonly interpreted as a transformation of bonding sequences.^[22] In our study, it is found that the hybridizations between the oxygen molecule and the surrounding tungsten atoms directly suppress the π^* peak. As shown in the top inset of Figure 2g, the real-space orbital distribution for the peak A resembles an orbital shape of the σ^* peak for the physisorbed oxygen molecule, indicating that the hybridizations between the oxygen molecule and the tungsten atoms induce σ^* antibonding energy state similar to that of the physisorbed oxygen molecule. In contrast, for the peak B, the real-space orbitals show highly delocalized distribution for both the oxygen molecule and the WS₂ crystal (the bottom inset of Figure 2g), implying that the peak B is due to the transition of the core electrons to continuum bands contributed from both the oxygen molecules and the WS₂ crystals.

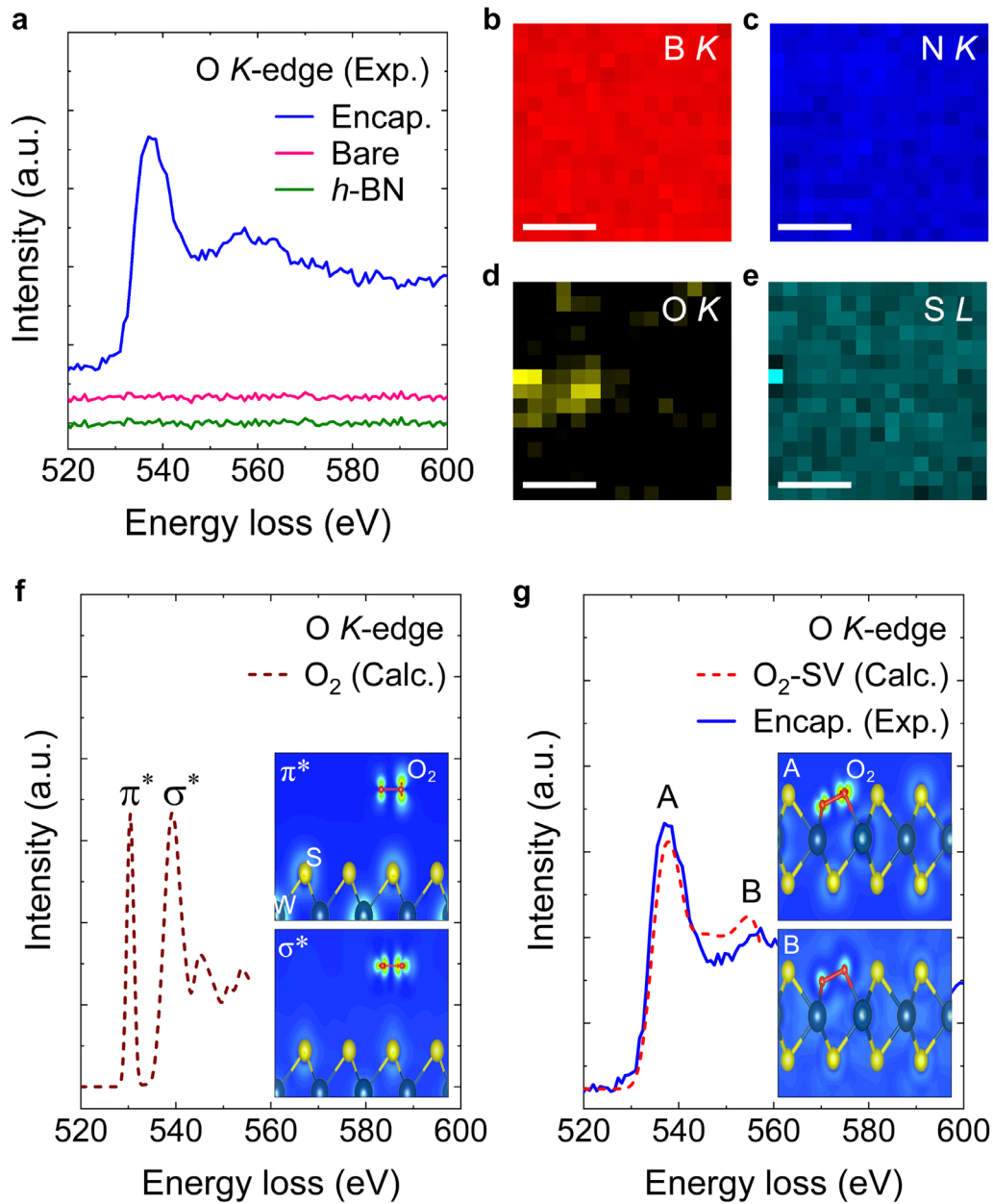


Figure 2. a) Experimental oxygen K -edge EELS spectra for the h -BN encapsulated WS_2 , bare WS_2 , and h -BN flake crystals. b-e) The EELS maps for the boron (b), nitrogen (c), oxygen (d) K -edge, and the sulfur (e) L -edge measured from h -BN encapsulated WS_2 . The scale bars are 100 nm. f) The calculated oxygen K -edge EELS spectrum $\epsilon_2(\omega)$ for a physisorbed oxygen molecule on the pristine WS_2 . g) The calculated oxygen K -edge EELS spectrum $\epsilon_2(\omega)$ (red dashed) for a chemisorbed oxygen molecule on the sulfur vacancy (O_2 -SV) of the WS_2 . The experimental oxygen K -edge spectrum (blue line) for the h -BN encapsulated WS_2 is in good agreement with the calculation result (red dashed). The insets of (f,g) represent the real-space orbital distributions $\rho(\mathbf{r})_E$ of the π^* ($E \approx 530$ eV) and σ^* ($E \approx 539$ eV) for (f) and the A ($E \approx 538$ eV) and B ($E \approx 555$ eV) for (g), respectively.

The investigation of the exciton recombination processes against the excitation power for the bare and *h*-BN encapsulated WS₂ crystals reveals that the oxygen fixation suppresses the nonradiative decay for the neutral excitons by stabilizing the free electron density of the WS₂. Figures 3a,b show the double-logarithmic plots of the neutral exciton (X⁰) emission intensity of the bare and *h*-BN encapsulated WS₂ crystals as a function of the excitation power density under ambient air and vacuum conditions at room temperature, respectively. The bare WS₂ crystal in air exhibits a sublinear increase with an exponent of 0.71 in a power-law ($I \propto P^\alpha$, P : excitation power), while that in vacuum shows a smaller exponent of 0.32. The power dependence can be understood by introducing a simple rate equation model for the steady-state photoluminescence. The rate equation for exciton generation and recombination can be described by^[23,24]

$$G = \frac{n_X}{\tau_X} + Tn_Xn_e + An_Xn_e + \gamma n_X^2 \quad (1)$$

where n_X is the neutral exciton density, τ_X is the exciton lifetime, n_e is the electron density, T is the trion formation coefficient, A is the exciton-electron Auger coefficient, and γ is the exciton–exciton annihilation coefficient. At our excitation power range, the exciton density is estimated to be from the low 10^{10} cm^{-2} to the low 10^{11} cm^{-2} . In this range of exciton density, it has been known that the exciton-exciton annihilation process becomes negligible.^[25] Furthermore, the recent work has shown that the photogenerated excitons are mostly converted to the trions in this range, indicating that the Auger process can also be neglected.^[24] Thus, the predominant nonradiative decay channel of the neutral excitons is the exciton-to-trion conversion process (see Figure S13 in Supporting Information). When the free electron density increases with the power dependence of P^μ , the neutral excitons are converted to the trions in proportional to P^μ , and the neutral exciton emission intensity follows the power-law of $P^{1-\mu}$ (see Supporting Information S12). The sublinear increase in the exciton emission in bare WS₂ indicates that the free electron density increases with increasing excitation power density by releasing oxygen molecules chemisorbed on defect sites, promoting the trion conversion process. The smaller exponent further confirms the easier desorption under ambient vacuum condition. Interestingly, the *h*-BN encapsulated WS₂ shows a linear increase with an exponent of 0.99 for both the air and vacuum ambient conditions, as shown in Figure 3b. This indicates that *h*-BN encapsulation results in predominant neutral exciton emission over the decay channels without generating free electrons by desorption.^[16,24] Figure 3c shows the photoluminescence intensity ratio (X^-/X^0) of the trion to the neutral exciton as a function of the excitation power density. The X^-/X^0 of bare WS₂ measured under ambient vacuum condition

steeply increases from 0.38 to 4.18, while the X^-/X^0 under the air environment gradually increases from 0.25 to 0.50 over the excitation power density range from 0.03 to 0.66 kW/cm². This further evidences that the desorption process, which induces free electrons and exciton-to-trion conversion, is much facilitated in vacuum than in air. In striking contrast, the X^-/X^0 of *h*-BN encapsulated WS₂ is kept almost constant at approximately 0.02 over the excitation power densities under both the ambient air and vacuum conditions, which is greatly reduced by more than one order of magnitude compared to that of the bare WS₂. This clearly indicates that *h*-BN encapsulation prevents the desorption of oxygen molecules by the laser illumination, resulting in predominant recombination by neutral excitons. By considering the intensity weight (I_{X^-}/I_{total}) of the trion in the photoluminescence spectra, we estimated the free electron density as a function of the excitation power density by using the mass action law (see Supporting Information S14).^[26,27] As shown in Figure 3d, the free electron density exhibits a very similar trend as X^-/X^0 . For bare WS₂, the free electron density drastically increases and reaches 2.66×10^{13} cm⁻² at an excitation power density of 0.66 kW/cm² in vacuum, which is close to the Mott density ($\sim 1 \times 10^{14}$ cm⁻²),^[28] while gradually increasing to 7.38×10^{12} cm⁻² at an excitation power density of 4.99 kW/cm² in air. However, regardless of the ambient conditions, the free electron density of *h*-BN encapsulated WS₂ is maintained at $\sim 9 \times 10^{10}$ cm⁻² with increasing excitation power, resulting from the fixation of chemisorbed oxygen molecules by *h*-BN layers. Additionally, using the bare and *h*-BN encapsulated WS₂ capacitor devices, we estimated the free electron densities in the bare and *h*-BN encapsulated WS₂ at the vacuum and air environments. For the bare WS₂, the electron densities were estimated to be 1.15×10^{13} cm⁻² (vacuum) and 3.69×10^{12} cm⁻² (air) at $V_g \cong 0$ V (gate voltage), respectively, while those of *h*-BN encapsulated WS₂ were estimated to be 2.05×10^{11} cm⁻² at both the vacuum and air environments. These electron densities were in good agreement with those estimated using the mass-action law. From the difference in free electron densities in-between the vacuum and air environments, we estimated the number of desorbed/adsorbed oxygen molecules on the sulfur vacancies to be 7.17×10^{12} cm⁻² (see Supporting Information S15).

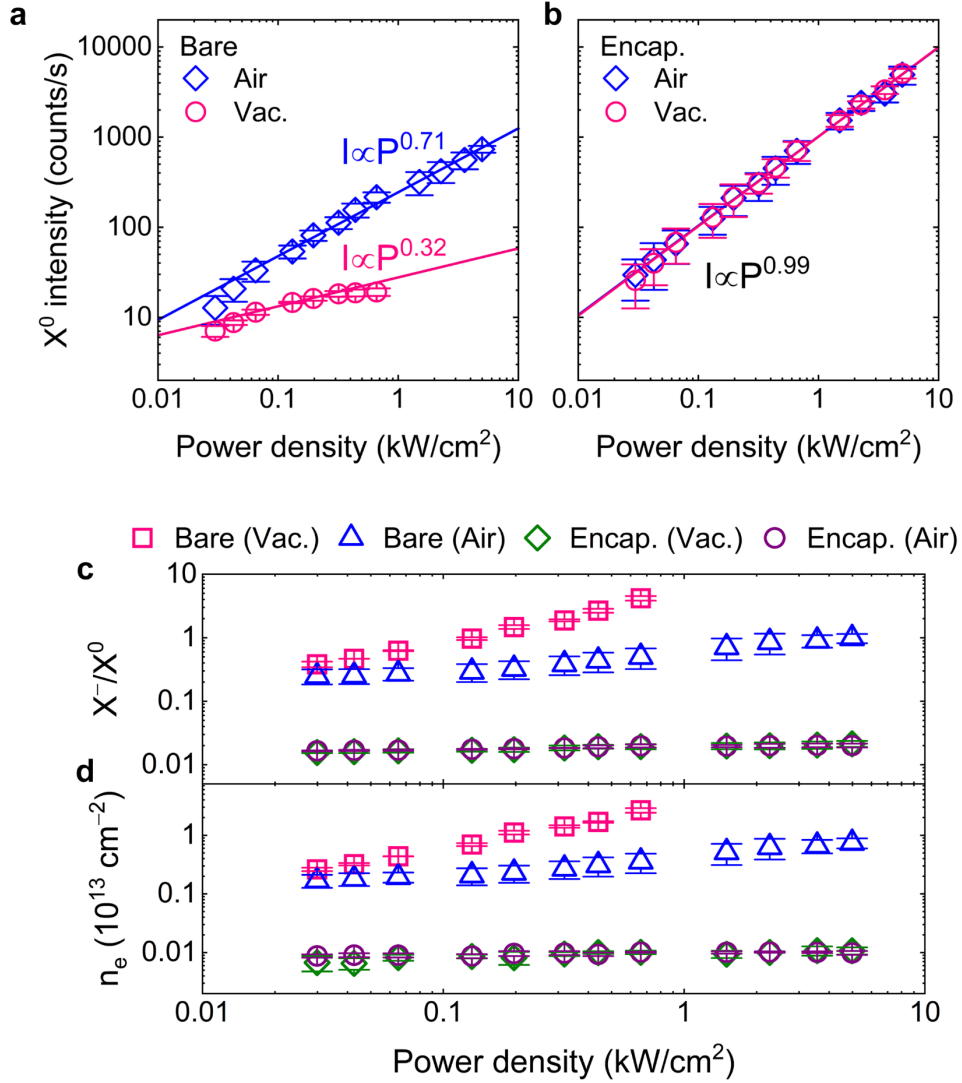


Figure 3. a,b) Neutral exciton (X^0) emission intensity of the bare (a) and *h*-BN encapsulated (b) WS₂ crystals as a function of the excitation power density at room temperature. The blue diamond and pink circle symbols indicate the power-dependent exciton emission intensity measured under ambient air and vacuum conditions. c) Photoluminescence intensity ratio (X^-/X^0) of the trion to the neutral exciton as a function of the excitation power density. d) Free electron density as a function of the excitation power density by using the mass action law. The pink square (blue triangle) and olive diamond (purple circle) symbols represent the X^-/X^0 and free electron density of the bare and *h*-BN encapsulated WS₂ under vacuum (air) ambient conditions, respectively. The error bars in (a–d) indicate the standard deviation of the measured data.

The nonradiative decay channel of neutral excitons can be attributed to exciton-to-trion conversion at our excitation power range. From the rate equation (1), the total recombination rate (R_T) can be described by $R_T = R_0 + R_A n_X$, where R_0 is the density-independent recombination rate and R_A is the exciton annihilation rate constant due to the exciton-to-trion conversion process. The role of the oxygen fixation can be quantitatively understood by estimating the exciton annihilation rate constant (R_A). To measure the exciton lifetime with increasing excitation power, we carried out time-resolved photoluminescence spectroscopy. For bare WS₂, the photoluminescence decay curves of neutral excitons under air ambient condition show a steep shortening of the decay time from 74 ps to 43 ps with increasing pump fluence from 27 to 959 nJ/cm², as shown in Figure 4a. However, the exciton decay curves for *h*-BN encapsulated WS₂ show a slight decrease in the lifetime above the pump fluence of 421 nJ/cm², as shown in Figure 4b. It is noteworthy that the exciton lifetime in *h*-BN encapsulated WS₂ becomes longer than that of bare WS₂, showing exciton lifetime of 136 ps in air at a pump fluence of 27 nJ/cm². The decay spectra at vacuum are shown in Figure S16 in Supporting Information. The increase in exciton lifetime in the *h*-BN encapsulated WS₂ strongly suggests that the nonradiative decay by the trion formation, which occurs on a very fast time scale of a few ps, is significantly inhibited due to the passivation of defects by the oxygen fixation.^[23,29,30] To quantitatively evaluate the exciton annihilation rate constant (R_A), the exciton density-induced recombination rate (τ^{-1}) was plotted as a function of the exciton density using the measured exciton lifetimes (see Supporting Information S17).^[30] Note that the exciton density was estimated by calculating the net absorption in the monolayer WS₂ for the pump fluence.^[31,32] As presented in Figures 4c,d, the *h*-BN encapsulated WS₂ crystals exhibit an exciton annihilation rate constant of $8.3 \times 10^{-3} \text{ cm}^2\text{s}^{-1}$ ($7.8 \times 10^{-3} \text{ cm}^2\text{s}^{-1}$), while the bare WS₂ crystals show a value of $8.0 \times 10^{-2} \text{ cm}^2\text{s}^{-1}$ ($3.2 \times 10^{-1} \text{ cm}^2\text{s}^{-1}$) under air (vacuum) ambient conditions. As expected, the exciton annihilation rate constant of the *h*-BN encapsulated WS₂ is remarkably reduced by approximately two orders of magnitude compared to that of the bare WS₂. These results are attributed to the suppression of exciton-to-trion conversion process in the *h*-BN encapsulated WS₂ due to the greatly lowered and stabilized free electron density. This fact can be additionally verified by investigating the decay dynamics of neutral excitons with an electrostatic doping in the *h*-BN encapsulated WS₂ capacitor devices at a fixed excitation power. Figure 4e shows the gate-voltage-dependent photoluminescence spectral map in the *h*-BN encapsulated WS₂ capacitor devices, showing that the charge neutral point is determined at $V_g \cong 0 \text{ V}$. The increase in the gate voltage ($V_g > 0 \text{ V}$) gives rise to the gradual decrease in the emission intensity for the neutral exciton and, simultaneously, the increase in the emission

intensity for the trion. This indicates that the increase in free electron density facilitates the exciton-to-trion conversion process, leading to the nonradiative decay of neutral excitons. The gate-voltage-dependent photoluminescence decay curves of neutral excitons also clearly show that the increase in the free electron density promotes the exciton annihilation. As shown in Figure 4f, the decay time of neutral excitons in the *h*-BN encapsulated WS₂ capacitor devices becomes steeply shorten from 139 ps to 36 ps for increasing the gate voltage from 0.5 V to 0.9 V. The exciton annihilation rate constant with the electrostatic doping is estimated to be $1.3 \times 10^{-1} \text{ cm}^2\text{s}^{-1}$ (see Supporting Information S18), which is similar to that of bare WS₂ under the vacuum ambient condition.

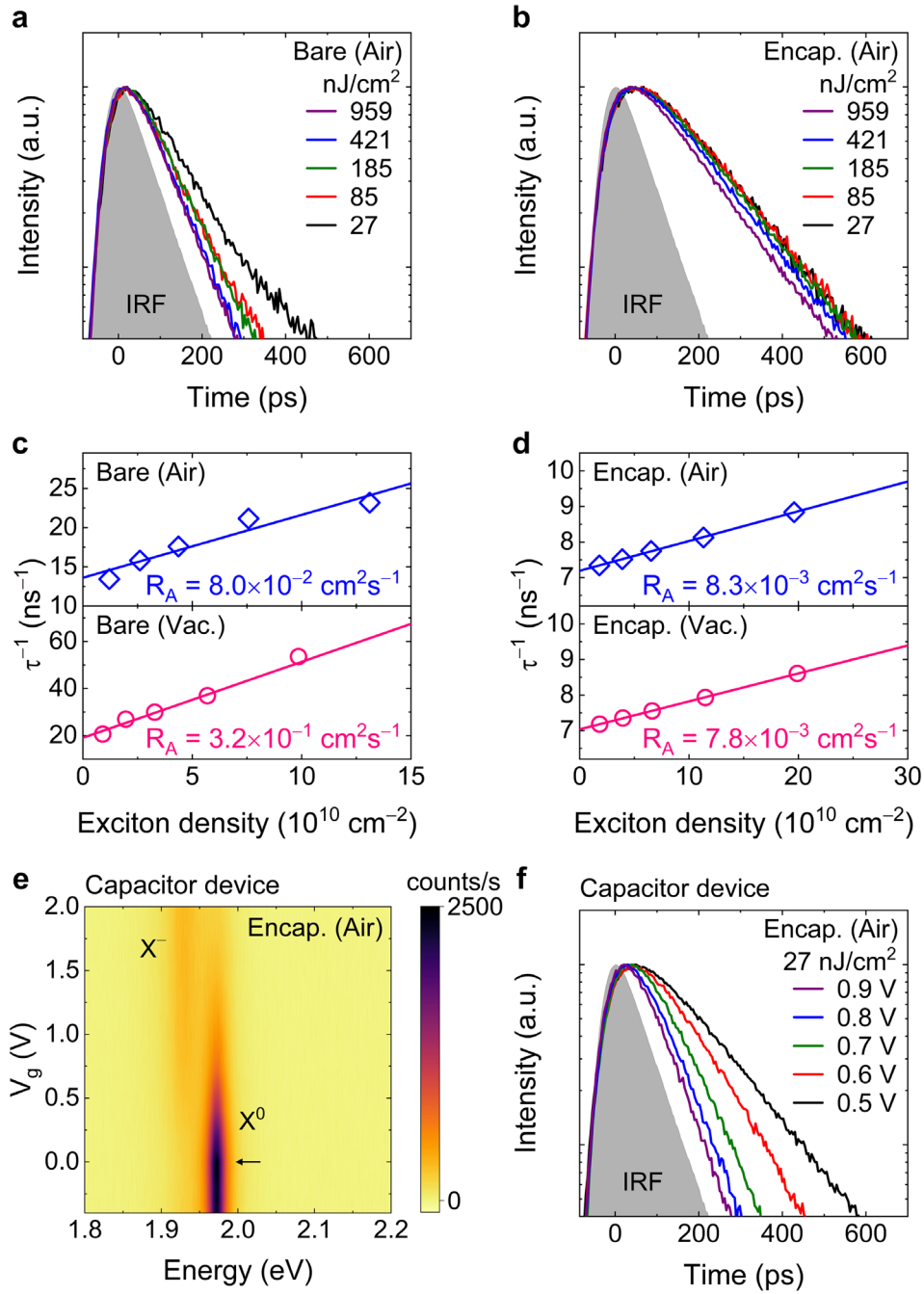


Figure 4. a,b) Photoluminescence decay curves of the neutral excitons measured as a function of the energy fluence for bare (a) and *h*-BN encapsulated (b) WS₂ under ambient air condition. c,d) Exciton density-induced recombination rate (τ^{-1}) for the bare (c) and *h*-BN encapsulated (d) WS₂ under ambient air and vacuum conditions, resulting in the exciton annihilation rate constant (R_A) due to exciton-to-trion conversion process by a linear fit. e) Gate-voltage-dependent photoluminescence spectral map of the *h*-BN encapsulated WS₂ capacitor devices. The black arrow indicates the charge neutral point of the *h*-BN encapsulated WS₂ capacitor device. f) Gate-voltage-dependent photoluminescence decay curves of the neutral excitons in the *h*-BN encapsulated WS₂ capacitor device.

The *h*-BN encapsulation gives rise to an almost constant level of the free electron density in WS₂ crystals for elevated excitation powers, which can provide a stable and robust valley polarization against various excitation conditions. In contrast, for bare WS₂, the drastic increase in free electron density with increasing excitation would cause a large variation in the valley polarization due to the change in decay dynamics of the neutral excitons caused by the exciton-to-trion conversion.^[33,34] To investigate the effect of *h*-BN encapsulation on the valley polarization, we carried out circular polarization-resolved photoluminescence measurements as a function of the excitation power density at 77 K. Figure 5a show the circularly polarized photoluminescence spectra measured from the bare (top panel) and *h*-BN encapsulated (bottom panel) WS₂, respectively. As a result, the degree of valley polarization with increasing excitation power shows a very different trend for the bare and *h*-BN encapsulated WS₂ crystals, as shown in Figure 5b. An important distinction is that the *h*-BN encapsulated WS₂ exhibits a stable valley polarization ratio at a constant level, whereas that of the bare WS₂ shows a large variation by changing the excitation power. The valley polarization can be described by the following equation $P_V = P_0 / (1 + 2\tau_X / \tau_V)$,^[35] where P_0 is the initial valley polarization, τ_X is the valley exciton lifetime, and τ_V is the valley relaxation time. The initial valley polarization (P_0) given by the optical selection rules can be assumed to be unity,^[5] meaning that the valley polarization (P_V) is then mainly governed by the competition between the exciton lifetime and the valley relaxation time.^[35] As shown in Figure 5b, the degree of valley polarization of bare WS₂ is 1.5 times higher than that of *h*-BN encapsulated WS₂ at the lowest excitation power density of 0.17 kW/cm². This can be attributed to the fact that in bare WS₂, the neutral excitons decay rapidly within the valley, rather than an intervalley scattering, due to a shortened exciton lifetime caused by a higher exciton-to-trion conversion rate. In addition, the large variation in the valley polarization of bare WS₂ can be understood as a result of the change in the exciton lifetime by the accelerated trion conversion process with increasing excitation power, as shown in Figures 4a and c.^[33,34] Accordingly, the valley polarization can be increased in the bare WS₂ for elevated excitation powers. For the *h*-BN encapsulated WS₂, however, the exciton-to-trion conversion and the exciton lifetime are maintained at almost constant levels, resulting in a stable valley polarization ratio for elevated excitation powers. The large variation in the valley polarization is also observed in the *h*-BN encapsulated WS₂ capacitor devices with the electrostatic doping (Figure 5c), showing the drastic decrease in the exciton lifetime as the gate voltage increases (see Supporting Information S19). This also confirms that the change in the free electron density leads to the large variation in the valley polarization.

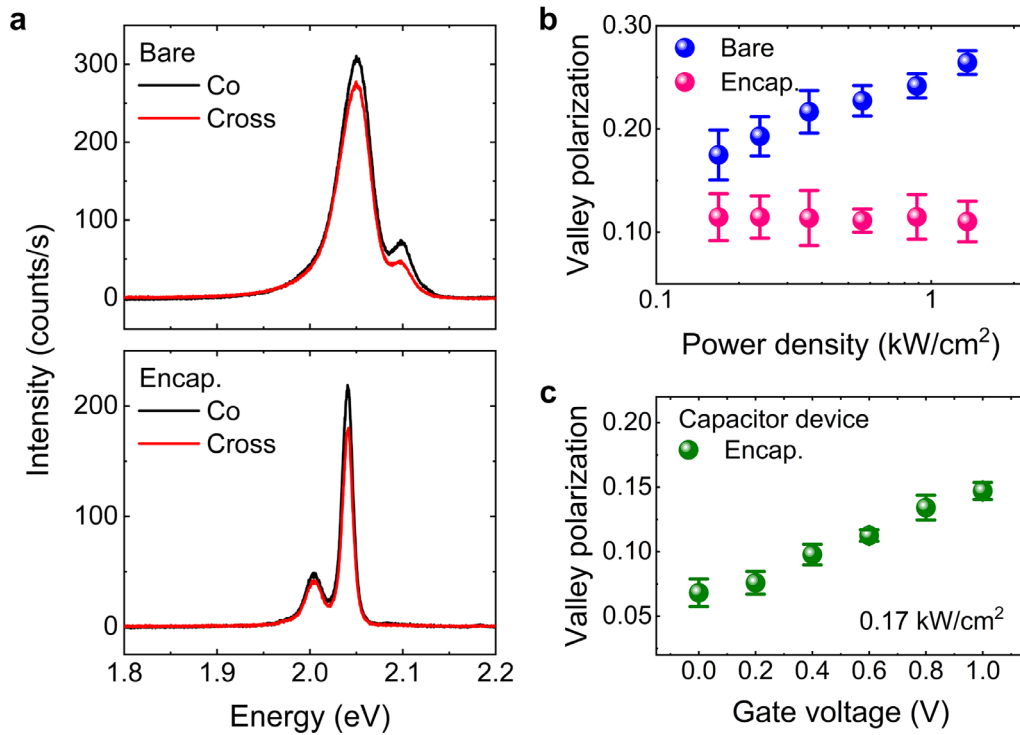


Figure 5. a) Circularly polarized photoluminescence spectra for the bare (top panel) and *h*-BN encapsulated (bottom panel) WS₂ measured at 77 K. b) Degree of valley polarization for the exciton emission in the bare and *h*-BN encapsulated WS₂ taken as a function of the excitation power density. c) Degree of valley polarization for the neutral excitons in the *h*-BN encapsulated WS₂ capacitor devices taken as a function of the gate voltage. The error bars marked in (b,c) exhibit the standard deviation of the measured valley polarization values.

3. Conclusion

In conclusion, we have demonstrated that *h*-BN encapsulation greatly removes the defect-related gap states by stabilizing the chemisorbed oxygen molecules onto the defects of monolayer WS₂ crystals, that are provided during the interactions between WS₂ and atmosphere. It is clearly shown that the oxygen molecules are chemisorbed onto the defects of WS₂ crystals and are fixated by *h*-BN encapsulation with excluding a possibility of oxygen molecules trapped in bubbles or wrinkles formed at the interface between WS₂ and *h*-BN, as confirmed by the EELS study. Optical spectroscopic studies show that *h*-BN encapsulation prevents the desorption of oxygen molecules over various excitation and ambient conditions, resulting in a greatly lowered and stabilized free electron density in monolayer WS₂ crystals. This suppresses the exciton annihilation processes by two orders of magnitude compared to that of bare WS₂. Furthermore, due to the stabilized free electron density in the *h*-BN encapsulated WS₂ crystals, the valley polarization becomes robust against the various excitation and ambient conditions. Our findings provide insight into the role of *h*-BN encapsulation and open up the possibility to control the defect states in 2D semiconductors through adsorbate-engineered 2D heterostructures.

4. Experimental Section

Sample preparation: The monolayer WS₂ crystals were grown on a sapphire substrate by chemical vapor deposition methods,^[19] and the *h*-BN flakes with a thickness of ~40 nm were prepared by mechanical exfoliations from bulk *h*-BN single crystals. The *h*-BN encapsulated WS₂ structure was fabricated by sequential pick-up processes using the dry van der Waals stacking method. Elvacite resin or polycarbonate (PC) was utilized as a polymer stamp for the pick-up of layered materials. The assembled *h*-BN/WS₂/*h*-BN structures and picked-up WS₂ crystals were released onto the line trenches by melting the polymer stamp, where the line trenches were fabricated through conventional photolithography and reactive ion etching processes using 400-nm-thick SiO₂-coated Si substrates. The polymer stamps were removed by immersing the fabricated sample in chloroform. Finally, both the *h*-BN encapsulated and the bare WS₂ onto line trenches were annealed at 350 °C to improve the coupling between the stacked layers and remove transfer residues.

Optical measurements: The steady-state and time-resolved photoluminescence measurements were performed using a home-built confocal microphotoluminescence system. Using a 40× (0.6 NA) objective (Nikon), the excitation beam was focused, and the signal from the samples was

collected through an optical fiber on the focal image plane. For the steady-state photoluminescence measurements, an argon-ion laser with a wavelength of 457.9 nm (continuous wave) was used as an excitation source. The photoluminescence spectra were resolved by a spectrometer (Acton SpectraPro 500i with 0.5 m focal length and 1200 grooves/mm grating) equipped with a charge-coupled device (CCD) detector (Princeton Instruments, 512×2048 pixels). For the circular polarization measurements, a combination of linear polarizer and quarter waveplate was used to generate circularly polarized excitation light, while another pair of linear polarizer and quarter waveplate was set for a polarization analyzer before collecting the signal through the slit of the spectrometer. The degree of valley polarization is defined as $\rho = [(PL(\sigma^+) - PL(\sigma^-)]/[PL(\sigma^+) + PL(\sigma^-)]$, where $PL(\sigma^\pm)$ are the photoluminescence intensity for σ^+ and σ^- polarized light components under excitation with a σ^+ or σ^- polarized laser beam. The time-resolved photoluminescence measurements were carried out using a picosecond pulsed diode laser (PicoQuant, LDH-P-FA-355) with a wavelength of 355 nm (FWHM = 56 ps) and repetition rate of 40 MHz. The exciton lifetimes were measured using a hybrid photomultiplier detector (PicoQuant, PMA hybrid series) and a time-correlated single photon counting system (PicoQuant).

Scanning transmission electron microscopy (STEM) and EELS analysis: STEM was used by Monochromated ARM-200F (NEO-ARM) in Korea Basic Science Institute (KBSI) operated at 200 kV. Gatan imaging filter (GIF) Continuum HR-1066 spectrometer was used to collect electron energy loss spectra.

Acknowledgements

This work was supported by the Basic Science Research Program (2019R1A2C1088525) and the BrainLink program (RS-2023-00236798) through the National Research Foundation of Korea, by the DGIST R&D Program (23-CoE-NT-01 and 23-HRHR+-03) funded by the Ministry of Science and ICT of the Korean Government. K.W. and T.T. acknowledge support from JSPS KAKENHI (Grant Numbers 19H05790, 20H00354 and 21H05233) and A3 Foresight by JSPS. Y.K. was supported by National Research Foundation of Korea (2020R1C1C1006914). J.H.J. and H.S.C. were supported by the Technology Innovation Program (20010542) funded by the MOTIE, Korea. The authors thank the computational support from the Center for Advanced Computation (CAC) at Korea Institute for Advanced Study (KIAS). Y.K. supported by a KIAS individual Grant (PG088601).

Keywords

chemisorption, defect passivation, hexagonal boron nitride, oxygen molecule, transition metal dichalcogenide

References

- [1] Y. You, X. X. Zhang, T. C. Berkelbach, M. S. Hybertsen, D. R. Reichman, T. F. Heinz, *Nat. Phys.* **2015**, *11*, 477.
- [2] J. G. Kim, W. S. Yun, S. Jo, J. Lee, C. H. Cho, *Sci. Rep.* **2016**, *6*, 29813.
- [3] C. Jin, E. C. Regan, A. Yan, M. I. B. Utama, D. Wang, S. Zhao, Y. Qin, S. Yang, Z. Zheng, S. Shi, K. Watanabe, T. Taniguchi, S. Tongay, A. Zettl, F. Wang, *Nature* **2018**, *567*, 76.
- [4] J. W. Jung, H. S. Choi, T. Lee, Y. J. Lee, S. H. Hong, J. W. Kang, C. H. Cho, *Appl. Phys. Lett.* **2021**, *119*, 143101.
- [5] K. F. Mak, K. He, J. Shan, T. F. Heinz, *Nat. Nanotechnol.* **2012**, *7*, 494.
- [6] D. Rhodes, S. H. Chae, R. Ribeiro-Palau, J. Hone, *Nat. Mater.* **2019**, *18*, 541.
- [7] Y. Yu, Y. Yu, C. Xu, Y. Q. Cai, L. Su, Y. Zhang, Y. W. Zhang, K. Gundogdu, L. Cao, *Adv. Funct. Mater.* **2016**, *26*, 4733.
- [8] C. R. Dean, A. F. Young, I. Meric, C. Lee, L. Wang, S. Sorgenfrei, K. Watanabe, T. Taniguchi, P. Kim, K. L. Shepard, J. Hone, *Nat. Nanotechnol.* **2010**, *5*, 722.
- [9] F. Cadiz, E. Courtade, C. Robert, G. Wang, Y. Shen, H. Cai, T. Taniguchi, K. Watanabe, H. Carrere, D. Lagarde, M. Manca, T. Amand, P. Renucci, S. Tongay, X. Marie, B. Urbaszek, *Phys. Rev. X* **2017**, *7*, 021026.
- [10] Y. Hoshi, T. Kuroda, M. Okada, R. Moriya, S. Masubuchi, K. Watanabe, T. Taniguchi, R. Kitaura, T. Machida, *Phys. Rev. B* **2017**, *95*, 241403(R).
- [11] J. Wierzbowski, J. Klein, F. Sigger, C. Straubinger, M. Kremser, T. Taniguchi, K. Watanabe, U. Wurstbauer, A. W. Holleitner, M. Kaniber, K. Müller, J. J. Finley, *Sci. Rep.* **2017**, *7*, 12383.
- [12] J. W. Kang, J. W. Jung, T. Lee, J. G. Kim, C. H. Cho, *Phys. Rev. B* **2019**, *100*, 205304.
- [13] X. Liu, D. Qu, L. Wang, M. Huang, Y. Yuan, P. Chen, Y. Qu, J. Sun, W. J. Yoo, *Adv. Funct. Mater.* **2020**, *30*, 2004880.
- [14] H. Liu, N. Han, J. Zhao, *RSC Adv.* **2015**, *5*, 17572.
- [15] Y. Liu, P. Stradins, S. H. Wei, *Angew. Chem. Int. Ed.* **2016**, *55*, 965.
- [16] H. Nan, Z. Wang, W. Wang, Z. Liang, Y. Lu, Q. Chen, D. He, P. Tan, F. Miao, X. Wang, J. Wang, Z. Ni, *ACS Nano* **2014**, *8*, 5738.

- [17] P. K. Gogoi, Z. Hu, Q. Wang, A. Carvalho, D. Schmidt, X. Yin, Y. H. Chang, L. J. Li, C. H. Sow, A. H. C. Neto, M. B. H. Breese, A. Rusydi, A. T. S. Wee, *Phys. Rev. Lett.* **2017**, *119*, 077402.
- [18] S. KC, R. C. Longo, R. M. Wallace, K. Cho, *Journal of Applied Physics* **2015**, *117*, 135301.
- [19] S. Jo, J. W. Jung, J. Baik, J. W. Kang, I. K. Park, T. S. Bae, H. S. Chung, C. H. Cho, *Nanoscale* **2019**, *11*, 8706.
- [20] G. Plechinger, P. Nagler, J. Kraus, N. Paradiso, C. Strunk, C. Schüller, T. Korn, *Phys. Status Solidi RPL* **2015**, *9*, 457.
- [21] T. Kato, T. Kaneko, *ACS Nano* **2016**, *10*, 9687.
- [22] Y. Shibasaki, Y. Kono, G. Shen, *Sci. Rep.* **2019**, *9*, 7531.
- [23] T. Kuechle, S. Klimmer, M. Lapteva, T. Hamzayev, A. George, A. Turchanin, T. Fritz, C. Ronning, M. Gruenewald, G. Soavi, *Opt. Mater. X* **2021**, *12*, 100097.
- [24] D. H. Lien, S. Z. Uddin, M. Yeh, M. Amani, H. Kim, J. W. A. III, E. Yablonovitch, A. Javey, *Science* **2019**, *364*, 468.
- [25] G. Moody, J. Schaibley, X. Xu, *J. Opt. Soc. Am. B.* **2016**, *33*, C39.
- [26] S. Mouri, Y. Miyauchi, K. Matsuda, *Nano Lett.* **2013**, *13*, 5944.
- [27] J. Siviniant, D. Scalbert, A. V. Kavokin, D. Coquillat, J. P. Lascaray, *Phys. Rev. B* **1999**, *59*, 1602.
- [28] A. Chernikov, C. Ruppert, H. M. Hill, A. F. Rigosi, T. F. Heinz, *Nat. Photonics* **2015**, *9*, 466.
- [29] A. Singh, G. Moody, K. Tran, M. E. Scott, V. Overbeck, G. Berghäuser, J. Schaibley, E. J. Seifert, D. Pleskot, N. M. Gabor, J. Yan, D. G. Mandrus, M. Richter, E. Malic, X. Xu, X. Li, *Phys. Rev. B* **2016**, *93*, 041401(R).
- [30] M. Kulig, J. Zipfel, P. Nagler, S. Blanter, C. Schüller, T. Korn, N. Paradiso, M. M. Glazov, A. Chernikov, *Phys. Rev. Lett.* **2018**, *120*, 207401.
- [31] J. W. Kang, B. Song, W. Liu, S. J. Park, R. Agarwal, C. H. Cho, *Sci. Adv.* **2019**, *5*, eaau9338.
- [32] H. L. Liu, C. C. Shen, S. H. Su, C. L. Hsu, M. Y. Li, L. J. Li, *Appl. Phys. Lett.* **2014**, *105*, 201905.
- [33] J. Carniggelt, M. Borst, T. V. D. Sar, *Sci. Rep.* **2020**, *10*, 17389.
- [34] Q. Zhang, H. Sun, J. Tang, X. Dai, Z. Wang, C. Z. Ning, *Nature Commun.* **2022**, *13*, 4101.
- [35] S. Feng, C. Cong, S. Konabe, J. Zhang, J. Shang, Y. Chen, C. Zou, B. Cao, L. Wu, N. Peimyoo, B. Zhang, T. Yu, *Small* **2019**, *15*, 1805503.

Supporting Information

Defect Passivation of 2D Semiconductors by Fixating Chemisorbed Oxygen Molecules via *h*-BN Encapsulations

*Jin-Woo Jung, Hyeon-Seo Choi, Young-Jun Lee, Youngjae Kim, Takashi Taniguchi, Kenji Watanabe, Min-Yeong Choi, Jae Hyuck Jang, Hee-Suk Chung, Dohun Kim, Youngwook Kim, and Chang-Hee Cho**

Jin-Woo Jung, Hyeon-Seo Choi, Young-Jun Lee, Dohun Kim, Youngwook Kim, Chang-Hee Cho

Department of Physics and Chemistry, Daegu Gyeongbuk Institute of Science and Technology (DGIST), Daegu 42988, South Korea

E-mail: chcho@dgist.ac.kr

Youngjae Kim

School of Physics, Korea Institute for Advanced Study (KIAS), Seoul 02455, South Korea

Takashi Taniguchi

International Center for Materials Nanoarchitectonics, National Institute for Materials Science, Tsukuba 305-0044, Japan

Kenji Watanabe

Research Center for Functional Materials, National Institute for Materials Science, Tsukuba 305-0044, Japan

Min-Yeong Choi, Jae Hyuck Jang, Hee-Suk Chung

Electron Microscopy and Spectroscopy Team, Korea Basic Science Institute, Daejeon 34133, South Korea

Jae Hyuck Jang

Graduate School of Analytic Science and Technology, Chungnam National University, Daejeon 34134, South Korea

S1. Kinetic barriers for O₂-chemisorption and O₂-dissociative chemisorption processes

We performed density functional theory calculations implemented in the quantum espresso code, employing Optimized Norm-Conserving Vanderbilt (ONCV) pseudopotentials and the nudged elastic band (NEB) methods for 3 by 3 superstructures of monolayer WS₂. These calculations, based on the grimme-D2 van der Waals corrections, reveal the relative energy evolution for each reaction path from the initial configurations to the final configurations.

Figures S1a and S1b show the kinetic barriers for the O₂-chemisorption and O₂-dissociative chemisorption processes in the monolayer WS₂ (a) and WTe₂ (b) with the sulfur vacancy (SV). In the case of the WS₂, the kinetic barrier for the O₂-chemisorption (0.56 eV) is lower than that for the O₂-dissociative chemisorption process (0.76 eV), as shown in Figure S1a. From the transition state theory, the reaction rate is given by $k \cong f \exp(-E_b/k_B T)$, where k is the reaction rate, f is the attempt frequency, E_b is the barrier, k_B is the Boltzmann constant, and T is the temperature. The attempt frequency can be approximated by the value of 10^{12} s^{-1} .^[1] The reaction rate ($T = 300 \text{ K}$) for the O₂-chemisorption and dissociative chemisorption processes is estimated to be approximately 180 s^{-1} ($E_b = 0.56 \text{ eV}$) and 0.17 s^{-1} ($E_b = 0.76 \text{ eV}$), respectively. This result indicates that the probability of the O₂-chemisorption is 1000 times higher than that of the O₂-dissociative chemisorption. Thus, the oxygen chemisorption on the monolayer WS₂ crystals would have the final configuration of the O₂-chemisorption rather than the O₂-dissociative chemisorption.^[2]

On the other hand, in the case of the WTe₂ (Figure S1b), there are no kinetic barriers (0.00 eV) for both the O₂-chemisorption and O₂-dissociative chemisorption processes, indicating that the oxygen chemisorption spontaneously occurs toward the O₂-dissociative chemisorption process in the case of WTe₂. These results are in good agreement with previous theoretical studies, showing that the type of the oxygen chemisorption depends on TMD materials.^[2]

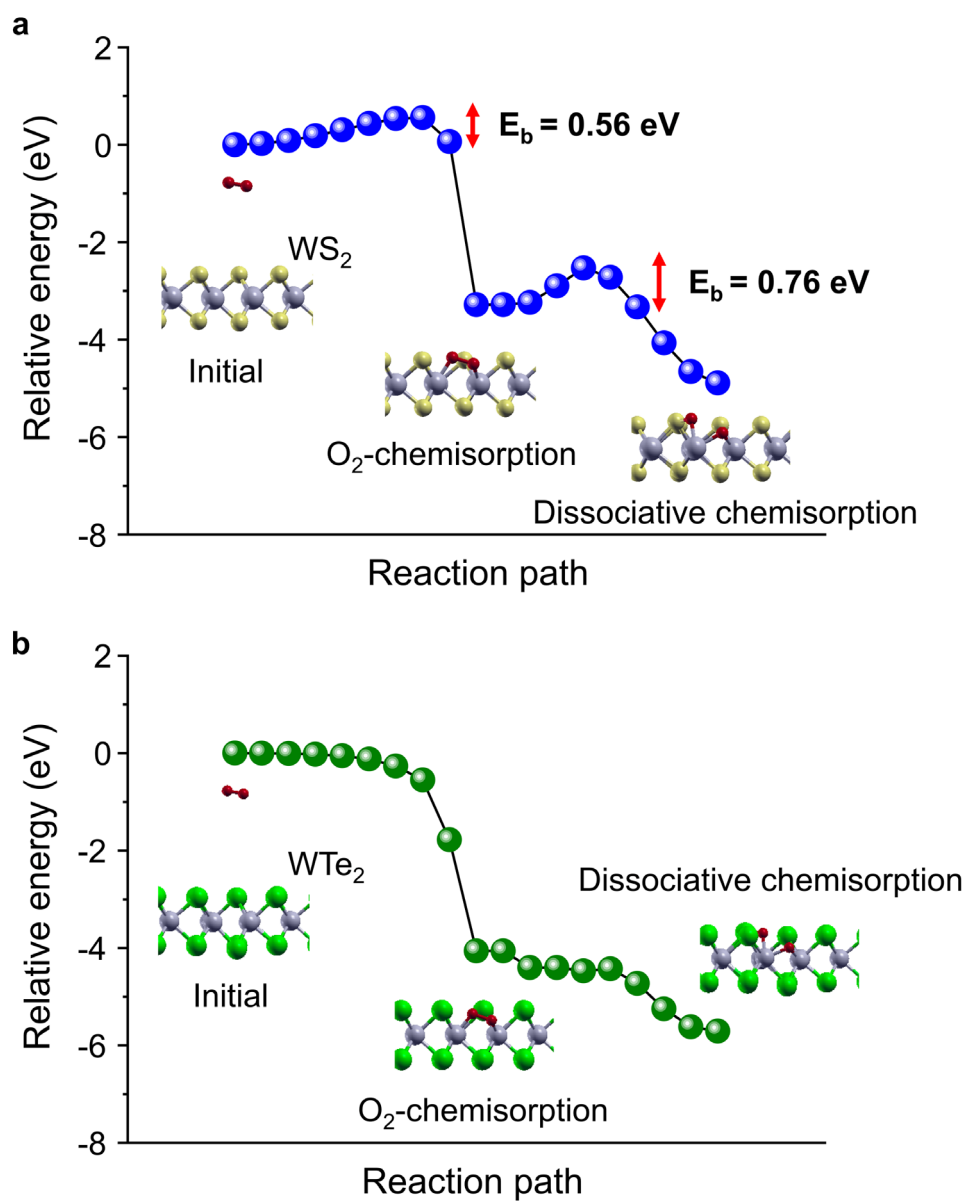


Figure S1. (a,b) Calculated reaction path and kinetic barriers for the O₂-chemisorption and O₂-dissociative chemisorption processes in the monolayer WS₂ (a) and WTe₂ (b) with the sulfur vacancy, respectively.

S2 and S3. Molecular interactions with the pristine surface and sulfur vacancy of WS₂

Figures S2 and S3 reveal the relative energy evolutions as a function of the reaction path for N₂, O₂, and H₂O with both the pristine WS₂ and SV of WS₂. In this reaction path, the decrease in relative energy indicates that the molecular adsorption proceeds toward a physisorption, corresponding to an exothermic process.^[3] Meanwhile, an increase in relative energy exhibits that the molecular adsorption proceeds toward a chemisorption, which leads to an activation barrier in the chemical bonding sequence.

As shown in Figure S2, the N₂ molecule does not achieve a structurally favorable state when chemisorbed onto the SV. However, the N₂ exhibits a preference for physisorption (−0.08 eV) just prior to forming a chemical bond with surrounding tungsten atoms. Conversely, the O₂ starting from a weakly physisorbed state displays a minor repulsive barrier of ~0.56 eV just before chemically bonding. Subsequently, it attains a fully stable chemisorption state with the SV site, resulting a favorable energy of −3.28 eV. On the other hand, the H₂O prefers a physisorption-like configuration with the SV of WS₂, which does not show a chemisorption configuration.

Figure S3 shows the first-principles NEB calculation results for the molecular interaction with pristine WS₂. In case of the physisorption, all three molecules can be weakly physisorbed with the pristine WS₂. However, the weak adsorption energies in the final states lead to unstable physisorption configurations, resulting in the easy desorption of physisorbed molecules on pristine WS₂ surface. Thus the physisorption has virtually no influence on the electronic and optical properties of the WS₂ monolayer.

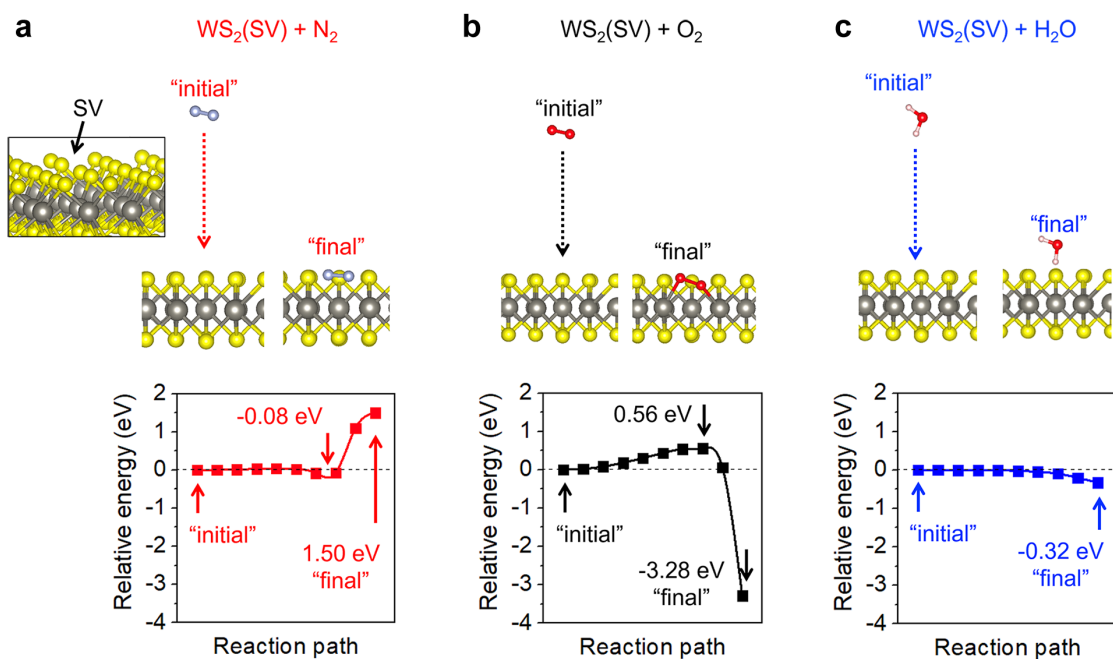


Figure S2. First-principles NEB calculations for molecular interactions with SV of WS₂. (a–c) The relative energy evolution of the N₂ (a), O₂ (b), and H₂O (c) for each reaction path from the initial configurations to the final configurations. The relative energy is defined as the total energy difference compared to that of the initial. Adsorption of a molecule at given surface has two different forms, physisorption and chemisorption. The physisorption reflects an exothermic process, resulting in a decrease in relative energy. The chemisorption, on the other hand, exhibits an activation barrier in the chemical bonding sequence, leading to an increase in relative energy. (a) The N₂ molecule does not achieve a structurally favorable chemisorption state when adsorbed onto the SV. (b) The O₂ molecule can be only chemisorbed onto the SV and attain a fully stable chemisorption state (−3.28 eV). (c) The H₂O molecule prefers a physisorption-like configuration with the SV of WS₂, which does not show a chemisorption.

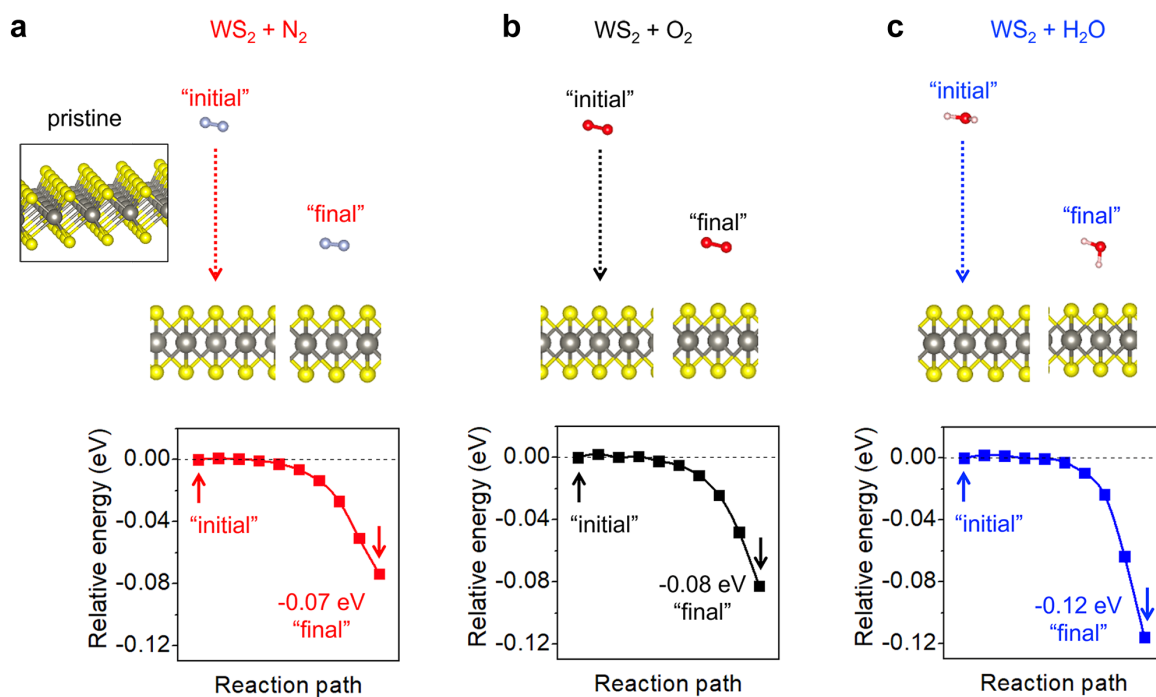


Figure S3. First-principles NEB calculations for molecular interactions with pristine WS₂. (a–c) The relative energy evolution of the N₂ (a), O₂ (b), and H₂O (c) for each reaction path from the initial configurations to the final configurations.

S4. Bare and *h*-BN encapsulated WS₂ suspended on the line trenches

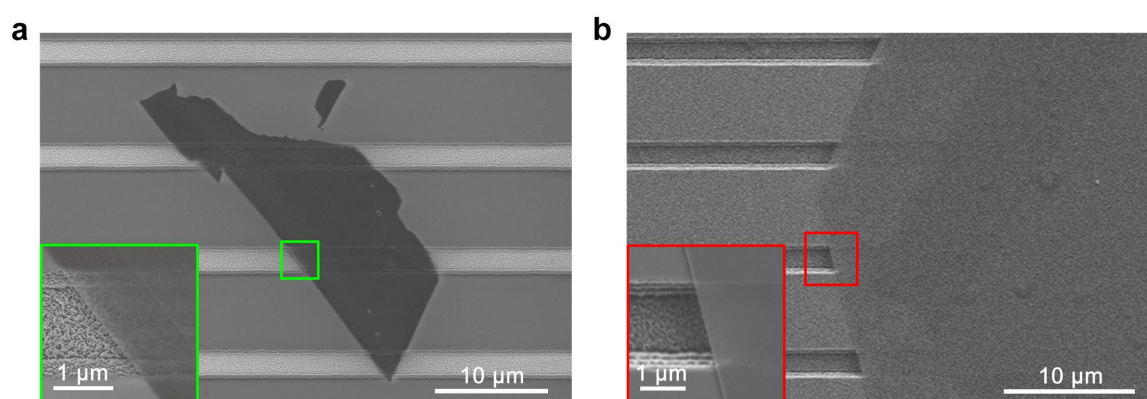


Figure S4. a,b) Scanning electron microscope images of the bare and *h*-BN encapsulated WS₂ crystals on the line trenches. The insets of (a) and (b) are the zoom-in images for the square marks of green and red boxes.

S5. Exciton species in the bare and *h*-BN encapsulated WS₂

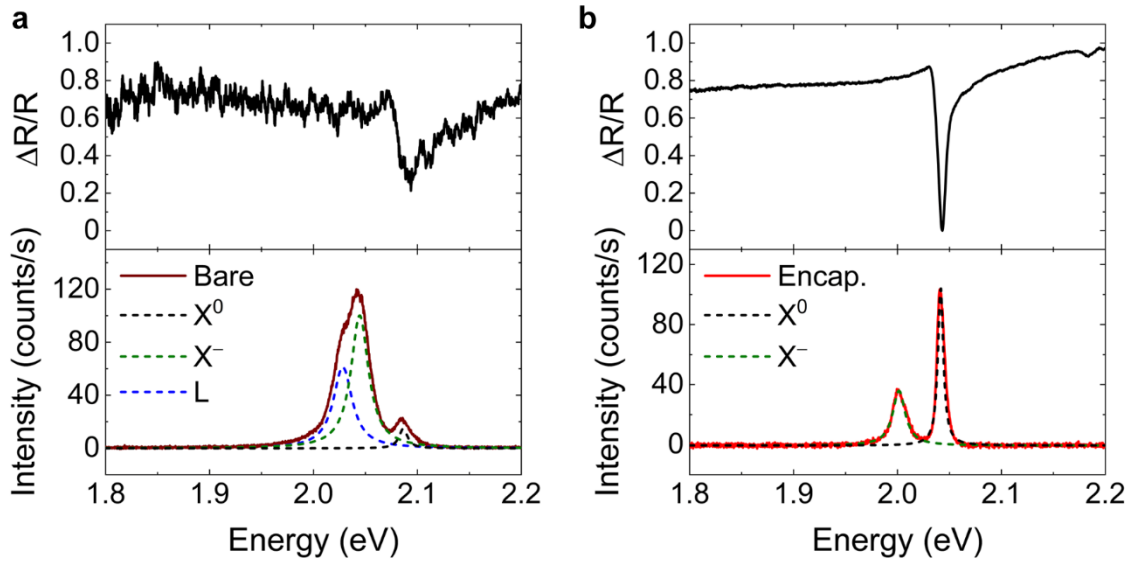


Figure S5. a,b) Differential reflectance and photoluminescence spectra measured from the bare (a) and *h*-BN encapsulated (b) WS₂ at the cryogenic temperature of 77 K. From the differential reflectance measurements, the exciton energy for the bare and *h*-BN encapsulated WS₂ was assigned to be 2.087 and 2.042 eV, respectively. By considering the peak separation between the exciton species based on the literatures,^[4,5] the photoluminescence spectrum for the bare WS₂ is deconvoluted to three excitonic species corresponding to the neutral exciton (X^0), trion (X^-), and defect-related trapped exciton (L) states at 2.087, 2.042, and 2.026 eV, respectively. For the *h*-BN encapsulated WS₂, the two exciton species are assigned to be the neutral exciton (X^0), trion (X^-) at 2.042 and 2.001 eV, respectively. Note that the redshift of the exciton and trion energy in the *h*-BN encapsulated WS₂ compared with the bare WS₂ is due to the increase in the dielectric constant of the environment by the *h*-BN encapsulation.^[6]

S6. Excitonic spectra of the bare and *h*-BN encapsulated WS₂ under the different ambient conditions

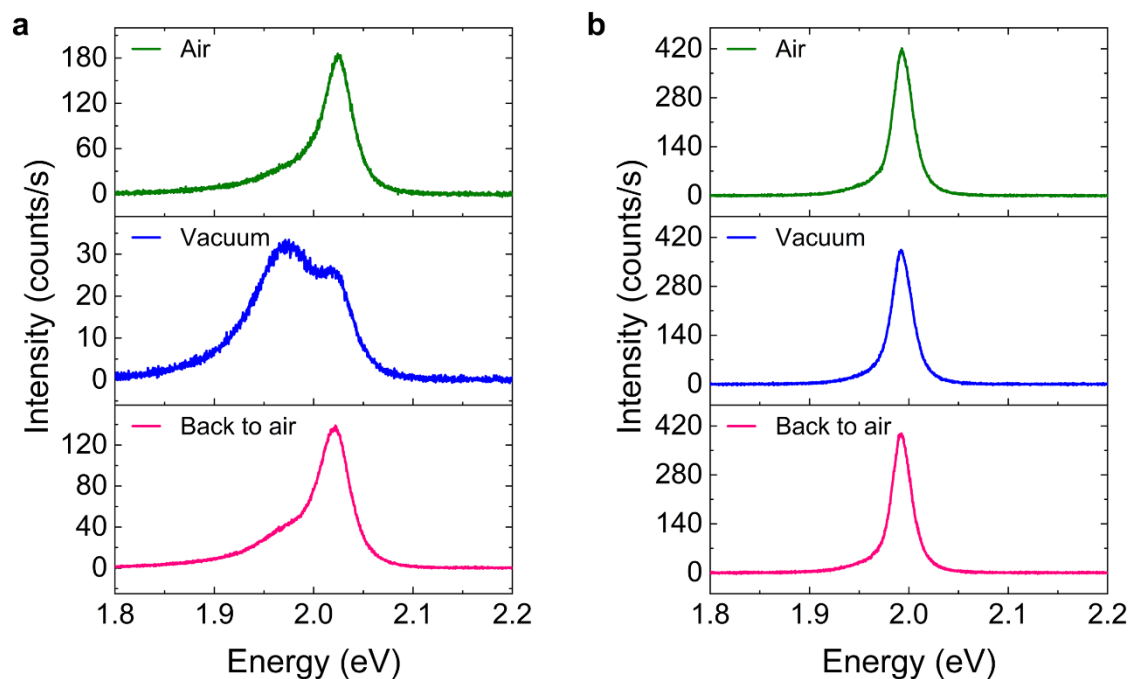


Figure S6. a,b) Photoluminescence spectra for the bare (a) and *h*-BN encapsulated (b) WS₂ measured under the ambient conditions of air, vacuum, and then air again. The photoluminescence spectral features of bare WS₂ are significantly altered according to the change in ambient condition, while those of *h*-BN encapsulated WS₂ are kept almost constant regardless of the change in ambient condition.

S7. *h*-BN encapsulated WS₂ fabricated under an inert gas environment

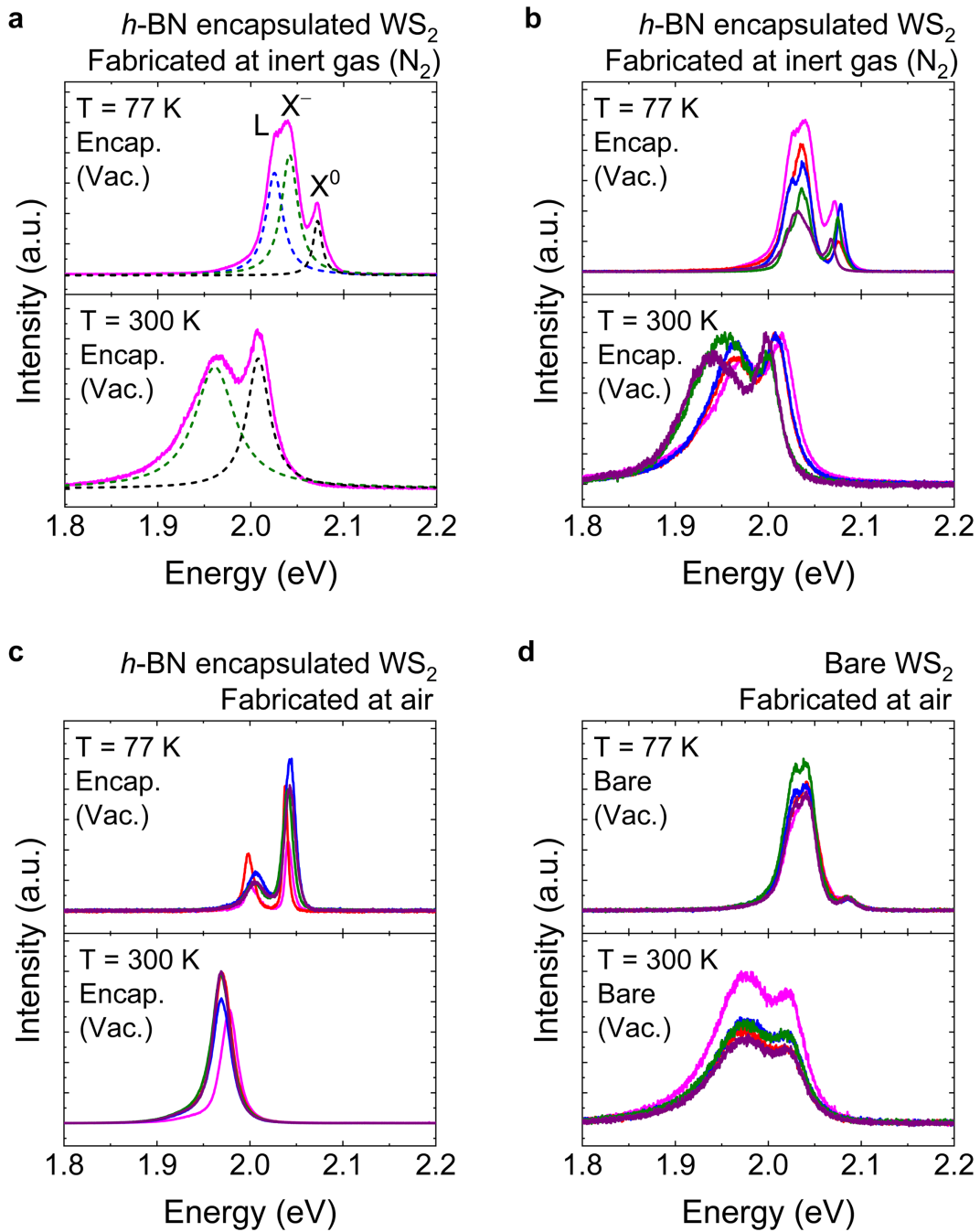


Figure S7. a) Photoluminescence spectra measured at the temperature of 77 K (top panel) and 300 K (bottom panel) for the *h*-BN encapsulated WS₂ fabricated under an inert environment. The black, olive, and blue dashed lines represent the neutral exciton (X⁰), trion (X⁻), and defect-related trapped exciton (L) states, respectively. b-d) Five representative spectra measured over many *h*-BN encapsulated WS₂ samples fabricated under the inert (b) and air (c) environments as well as the bare WS₂ (d) fabricated under the air environment.

S8. Spectral change in the exfoliated monolayer WS₂ and WSe₂ with a lower density of chalcogen vacancies by varying the ambient conditions

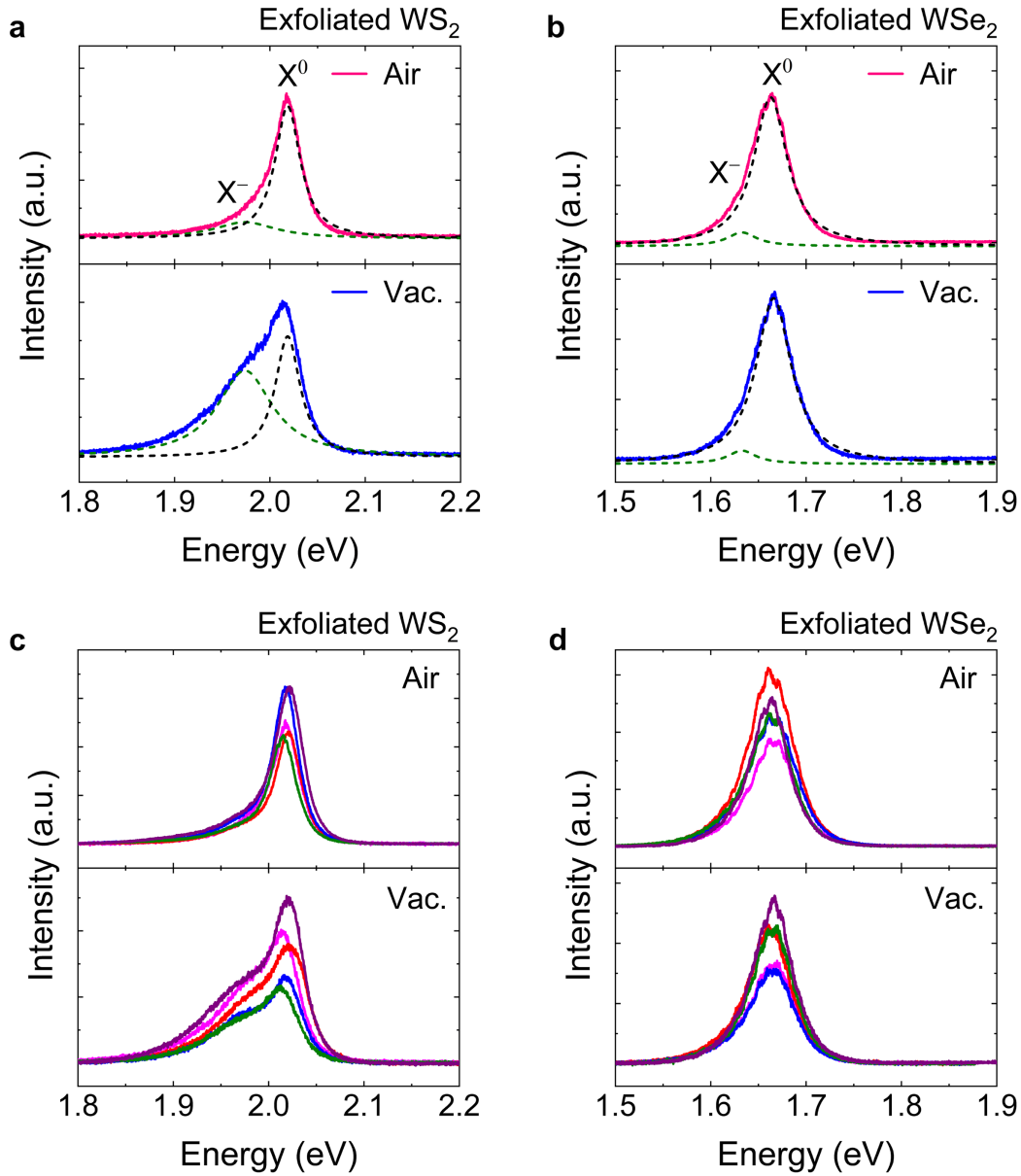


Figure S8. a,b) Photoluminescence spectra measured under the air (top panel) and vacuum (bottom panel) ambient conditions for the exfoliated monolayer WS₂ (a) and WSe₂ (b). The black and olive dashed lines represent the neutral exciton (X⁰) and trion (X⁻), respectively. c,d) Five representative spectra showing almost the same features over many WS₂ (c) and WSe₂ (d) samples under the variation of the air (top panel) and vacuum (bottom panel) ambient conditions.

S9. Electron energy loss spectroscopy spectra

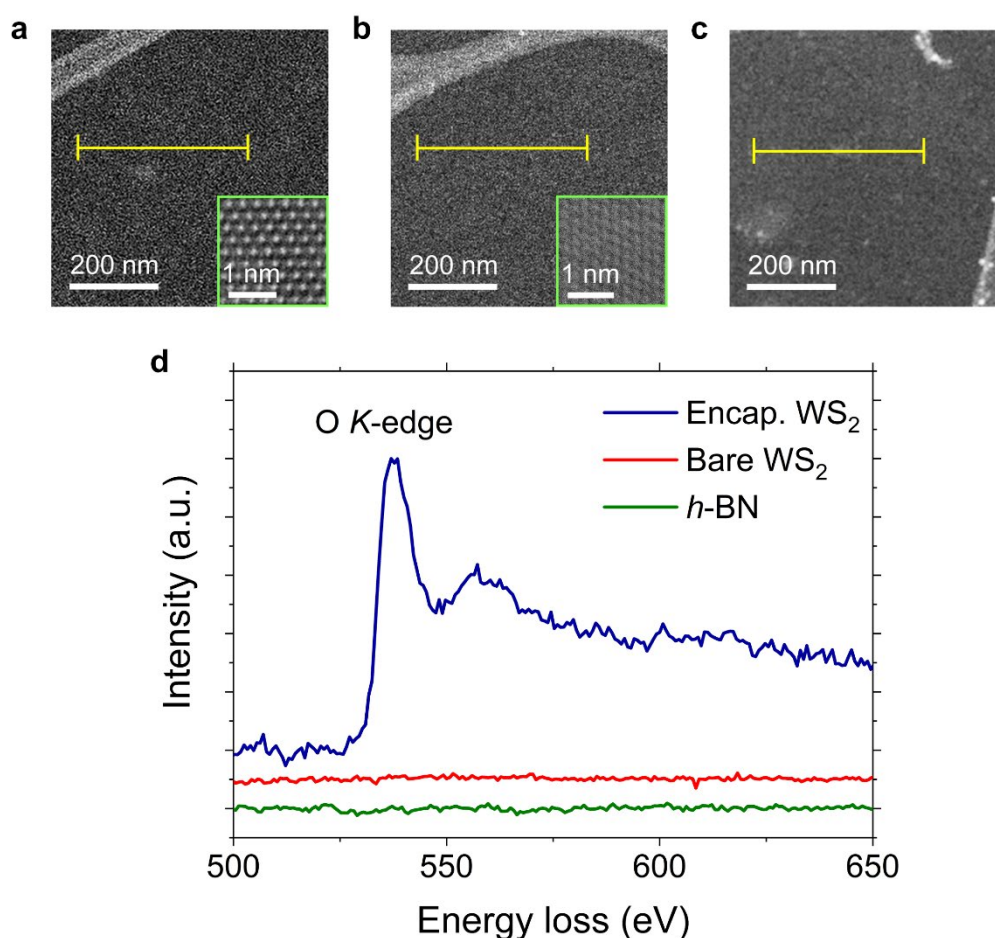


Figure S9. a–c) Annular dark field (ADF)-scanning transmission electron microscopy (STEM) images for bare WS₂ (a), *h*-BN flake (b), and *h*-BN encapsulated WS₂ crystals (c). Insets of (a,b) present the atomic-resolution ADF-STEM images for the bare WS₂ and *h*-BN flake. d) Oxygen *K*-edge electron energy loss spectroscopy (EELS) spectra for the *h*-BN encapsulated WS₂, bare WS₂, and *h*-BN flake. The EELS spectra are obtained from line-scanning for the regions (0.4 μm) marked as yellow bars in (a–c), and are acquired for a dwell time of 0.04 s per pixel. Note that in the case of the *h*-BN encapsulated WS₂, the strong boron and nitrogen signals in a few-nanometer-thick top and bottom *h*-BN layers encapsulating monolayer WS₂ interfere with the ability to obtain clear atomic-resolution STEM images of the monolayer WS₂. This makes it very challenging to clearly visualize the WS₂ plane in STEM images for *h*-BN encapsulated WS₂. More importantly, directly observing light atoms such as oxygen is challenging due to their easy knockout under the electron beam irradiation as well as the very weak TEM contrast, as widely reported in the previous works.^[7,8]

S10. Electron energy loss spectroscopy maps for *h*-BN encapsulated WS₂

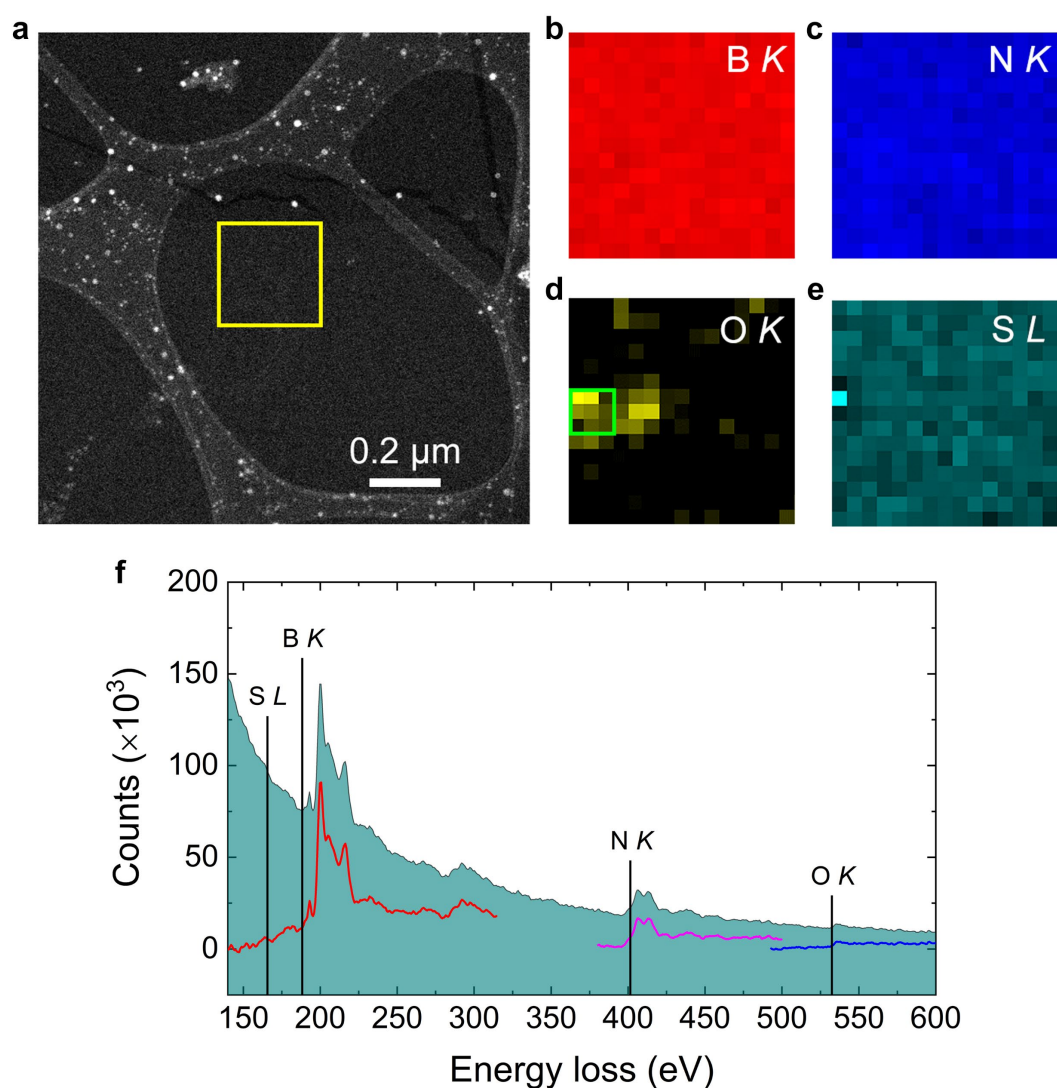


Figure S10. a) ADF-STEM image for the *h*-BN encapsulated WS₂ crystals. b-e) The EELS maps for the boron (b), nitrogen (c), oxygen (d) *K*-edge, and the sulfur (e) *L*-edge measured at the region marked by the yellow square box in (a). f) EELS spectrum measured at the region indicated by the green square box in (e).

S11. Theoretical calculation for EELS analysis

DFT calculation We employ the first-principles density functional theory implemented in the full-potential linearized plane wave (FLAPW) with local orbitals with the ELK code.^[9] In the calculation, the local-density approximation exchange correlation functional is adopted and size of basis set, rgkmax, is set to 7.0. $6 \times 6 \times 1$ \mathbf{k} -point grids are considered for WS₂ (2, 2) supercell with lattice constant of 3.13 Å.^[10,11] To consider core-hole excitation state, we perform the pseudo core-hole approach for a local orbital of orbital angular momentum $l = 0$, i.e., for the K -shell, in the FPLAPW with deep linearization energy (-25 atomic unit). The pseudo core-hole is made of one of the oxygen nuclei becomes positively charged ($+1e$) in the all-electron potential together with an additional electron ($-1e$) simultaneously created at the valence Kohn-Sham orbitals. After the first-principles self-consistent calculation, interactions between all the Kohn-Sham states in the unit-cell and the core-hole become properly demonstrated. The notation of Kohn-Sham Hamiltonian $\hat{H}_{ks}[\rho]$ and eigenstates $|\mathbf{k}, n\rangle$ with core-hole of oxygen K -edge can be rewritten as $\hat{H}_{ks}[\rho; O_i]|\mathbf{k}, n; O_i\rangle = E_{n,\mathbf{k}}|\mathbf{k}, n; O_i\rangle$. The $|\mathbf{k}, n; O_i\rangle$ stands for the Kohn-Sham eigenket at a band index n with \mathbf{k} momentum. The O_i indicates that the DFT calculation is performed under the Hamiltonian including a core-hole is created at given i th oxygen atom of the oxygen molecule ($O_2: O_{i=1}O_{i=2}$).

EELS calculation and Orbital distribution The EELS can be directly obtained via the following relation,

$$\epsilon_2(\omega; O_i) \sim \sum_{n,m,\mathbf{k}} f_{\mathbf{k},m}(2 - f_{\mathbf{k}+\mathbf{q},n})|\langle \mathbf{k} + \mathbf{q}, n; O_i | e^{i\mathbf{q}\cdot\mathbf{r}} | \mathbf{k}, m; O_i \rangle|^2 \delta(E_{n,\mathbf{k}+\mathbf{q}} - E_{m,\mathbf{k}} - \omega)$$

The $f_{\mathbf{k},n}$ represents occupation number of electrons. In the above relation, the $|\mathbf{k}, m; O_i\rangle$ should be an oxygen K -shell state of the i th oxygen atom. We define the direction of unit \mathbf{q} is approximately aligned along the in-plane cell vectors. The orbital distribution corresponding to each EELS peak can be extracted by following relation, $\rho(\mathbf{r}, O_i)_E = \sum_n |\langle \mathbf{r} | \mathbf{k}, n; O_i \rangle|^2 \delta(E - E_{n,\mathbf{k}} - E_K)$, here E_K is the energy of given core-hole K -shell of O_i with constant scissor operator. Note, in the Figure 2(b) of the manuscript, the x-ray absorption for physisorbed oxygen molecules provides identical transition pathways for $\epsilon_2(\omega; O_{i=1})$ and $\epsilon_2(\omega; O_{i=2})$ equivalently so that $\rho(\mathbf{r})_E \rightarrow \rho(\mathbf{r}; O_{i=1})_E$ and $\epsilon_2(\omega) \rightarrow \epsilon_2(\omega; O_{i=1})$ are displayed. For the chemisorbed oxygen molecules in the Figure 2(c) of the manuscript, however, each oxygen is not equivalent to each other. Thus we show the averaged EELS including two number of cases for core-hole excitations, say, $\epsilon_2(\omega) \rightarrow \epsilon_2(\omega; O_{i=1}) + \epsilon_2(\omega; O_{i=2})$ and $\rho(\mathbf{r})_E \rightarrow \rho(\mathbf{r}; O_{i=1})_E$. We will provide the $\rho(\mathbf{r}; O_{i=2})_E$ in the Figure S11.

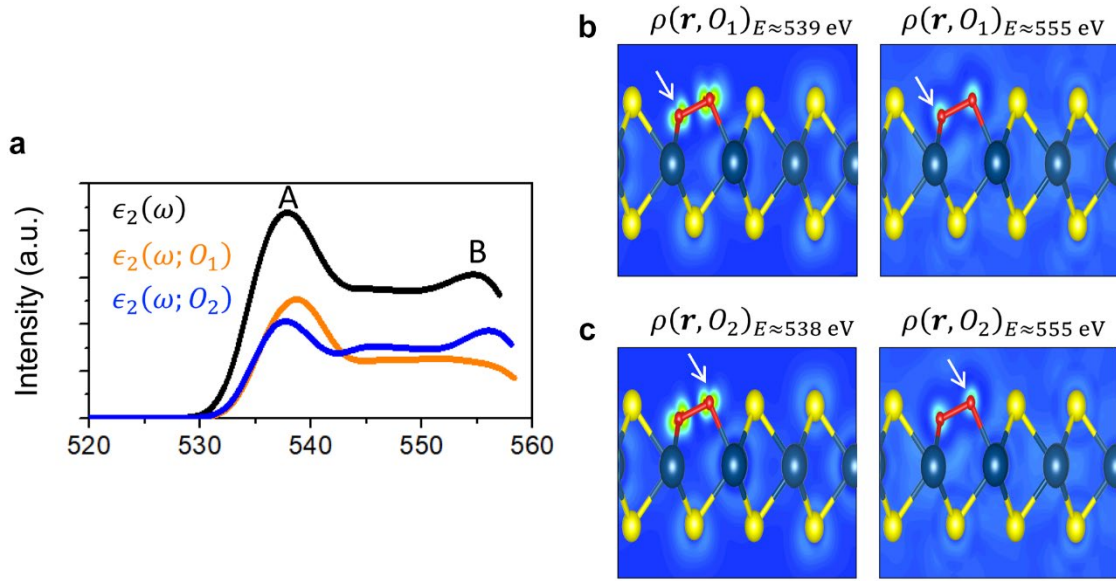


Figure S11. Core-hole dependent EELS spectra and orbital distributions. As long as chemisorbed, the two oxygens are not equivalent to each other and oxygen-dependent core-hole states become distinguishable. Here we assume that the experimental EELS is equally induced from the two kinds of oxygen core-holes. a) core-hole decomposed EELS, $\epsilon_2(\omega) = \epsilon_2(\omega; O_1) + \epsilon_2(\omega; O_2)$, and the $\epsilon_2(\omega)$ is displayed in the Figure 2(c) of the main text. b,c) The $\rho(r, O_i)$ for each peak, A and B, are displayed. White arrows indicate the oxygen atom with core-hole, i.e., $O_{i=1}$ (b) and $O_{i=2}$ (c). The peak A (black) at 538 eV can be decomposed into the two independent peaks at 537.7 eV (blue) and 538.7 eV (yellow). The physical origin of these decomposed peaks is found to be similar as depicted in the (b) and (c). However, the peak B at 555 eV is mostly contributed from that of the $\epsilon_2(\omega; O_2)$.

S12. Power-law for the neutral exciton emission intensity at room temperature

The exciton generation and recombination in the steady-state photoluminescence can be described by the following rate equation:^[12]

$$G = \frac{n_X}{\tau_X} + Tn_Xn_e + An_Xn_e + \gamma n_X^2 \quad (1)$$

where G is the exciton generation rate, n_X is the neutral exciton density, τ_X is the exciton lifetime, n_e is the electron density, T is the trion formation coefficient, A is the exciton-electron Auger coefficient, and γ is the exciton–exciton annihilation coefficient. Note that the contribution of localized excitons and dark excitons can be neglected by the thermal activation effect at room temperature.^[13,14] The exciton-electron Auger (An_Xn_e) and exciton-exciton annihilation (γn_X^2) processes can be neglected at a low level of excitation, and thus the exciton-to-trion conversion process becomes a dominant nonradiative decay at our experimental conditions. When the neutral exciton and free electron density increase with increasing the excitation power density (for the bare WS₂), the equation (1) can be simplified as the following equation:

$$G \cong Tn_Xn_e \quad (2)$$

When the free electron density increases with the power dependence of P^μ ($n_e \sim P^\mu$), the neutral exciton density can be written by

$$n_X \cong \frac{G^{1-\mu}}{T} \quad (3)$$

where the exciton generation rate is proportional to the excitation power ($G \propto P$). The neutral exciton emission intensity for the excitation power can be expressed as the following relation (4), showing that the neutral exciton emission intensity follows the power-law of $P^{1-\mu}$.

$$PL = \frac{n_X}{\tau_X} \cong \frac{G^{1-\mu}}{\tau_X T} \propto P^{1-\mu} \quad (4)$$

S13. Neutral exciton-to-trion conversion in the bare and *h*-BN encapsulated WS₂

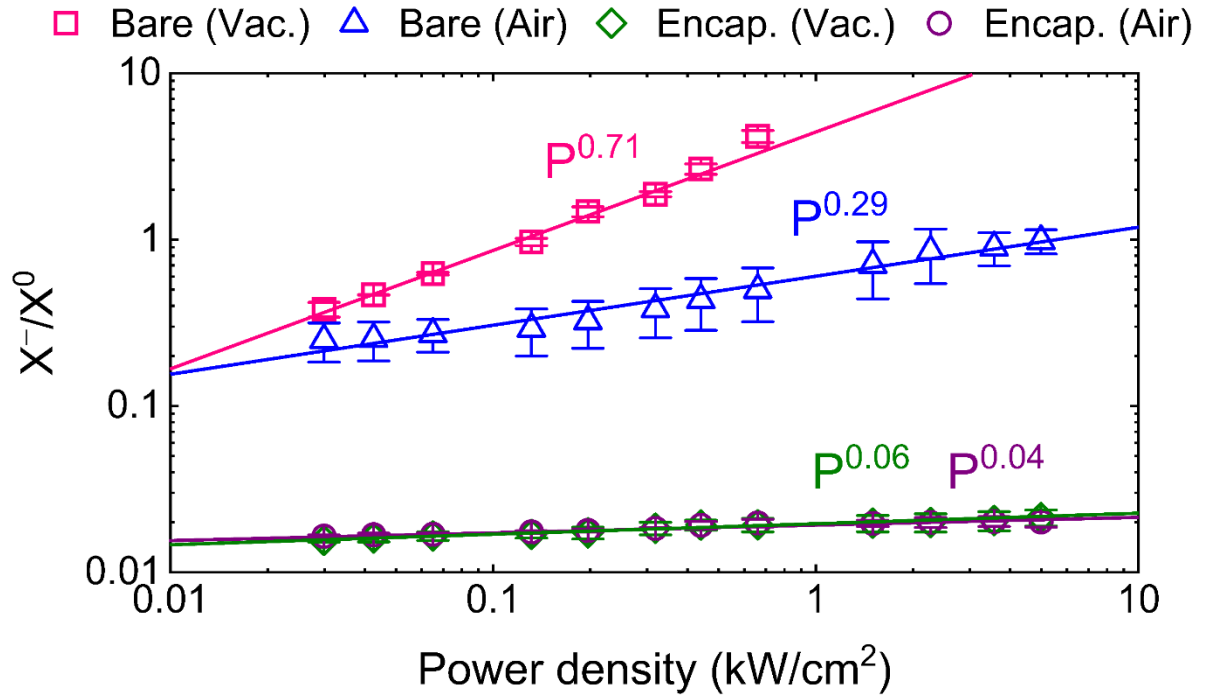


Figure S13. Photoluminescence intensity ratio (X^-/X^0) of the trion to the neutral exciton with increasing the excitation power density. In a power-law ($X^-/X^0 \propto P^\mu$), for the bare WS₂, the neutral excitons are converted to the trions in proportional to P^μ with the exponent μ of 0.71 and 0.29 in the ambient vacuum and air conditions with increasing the excitation power, while showing the exponent of 0.06 and 0.04 for the *h*-BN encapsulated WS₂ in the vacuum and air ambient conditions, respectively. As shown in Figures 3(a,b), the exciton emission intensity in the bare and *h*-BN encapsulated WS₂ increases with the exponent $\alpha \cong 1 - \mu$ under the vacuum and air conditions, indicating that the neutral exciton-to-trion conversion is the predominant process in the nonradiative decay of the excitons. Thus, Auger recombination process can be neglected under our excitation conditions.

S14. Estimation of the free electron density using mass action law

To determine the free electron density in the bare and *h*-BN encapsulated WS₂, we used the mass action law describing the formation of the trion (X^-) from the neutral exciton (X^0) and the free electrons (e). The formation of trion can be expressed by the following chemical equation:^[15,16]



From the chemical equation, the density of each carrier can be related by

$$\frac{n_{X^-}}{n_{X^0}} = \frac{n_e}{K(T)} \quad (2)$$

where n_{X^-} , n_{X^0} , and n_e correspond to the density of trions, neutral excitons, and electrons. $K(T)$ is the temperature-dependent equilibrium constant defined by the following equation:

$$K(T) = \left(\frac{4m_{X^0}m_e}{\pi\hbar^2m_{X^-}} \right) k_B T \exp\left(-\frac{E_b^{X^-}}{k_B T}\right) \quad (3)$$

where m_{X^-} , m_{X^0} , and m_e are the effective mass of the trion, neutral exciton, and electron. The effective mass of the trion and neutral exciton was calculated to be $1.33m_0$ ($m_{X^-} = 2m_e + m_h$) and $0.89m_0$ ($m_{X^0} = m_e + m_h$), where m_0 is the electron mass, m_e ($0.44m_0$) is the effective mass of the electron, m_h ($0.45m_0$) is the effective mass of the hole, k_B is the Boltzmann constant, T is the temperature, and $E_b^{X^-}$ is the trion binding energy (~ 34 meV).^[17,18]

By using the equations (2) and (3), we can obtain the following parameter:

$$\frac{n_{X^0}n_e}{n_{X^-}} = \left(\frac{4m_{X^0}m_e}{\pi\hbar^2m_{X^-}} \right) k_B T \exp\left(-\frac{E_b^{X^-}}{k_B T}\right) = 3.41 \times 10^{12} \text{ cm}^{-2} \quad (4)$$

The intensity weight (I_{X^-}/I_{Total}) of trions in the photoluminescence spectra measured from the bare and *h*-BN encapsulated WS₂ crystals can be written by the following equation:

$$\frac{I_{X^-}}{I_{total}} = \frac{\gamma_{X^-}n_{X^-}}{\gamma_{X^0}n_{X^0} + \gamma_{X^-}n_{X^-}} = \frac{\frac{\gamma_{X^-}n_{X^-}}{\gamma_{X^0}n_{X^0}}}{1 + \frac{\gamma_{X^-}n_{X^-}}{\gamma_{X^0}n_{X^0}}} \quad (5)$$

where γ_{X^0} and γ_{X^-} are the decay rate of neutral excitons and trions, respectively. $\gamma_{X^-}/\gamma_{X^0}$ was estimated by measuring the lifetimes of neutral excitons and trions.

By comparing the parameter (4) and the equation (5), we can obtain the following equation:

$$n_e = 3.41 \times 10^{12} \frac{\left(\frac{\gamma_{X^0}}{\gamma_{X^-}}\right) \left(\frac{I_{X^-}}{I_{total}}\right)}{\left(1 - \frac{I_{X^-}}{I_{total}}\right)} [\text{cm}^{-2}] \quad (6)$$

From the photoluminescence spectra measured as a function of the excitation power density, we estimated the free electron density in the bare and *h*-BN encapsulated WS₂ crystals.

S15. Quantitative estimate for the number of desorbed/adsorbed oxygen molecules on sulfur vacancies in-between the vacuum and air environments

To investigate a quantitative estimate of the adsorption/desorption of oxygen molecules on WS₂, we fabricated the bare WS₂ capacitor device (Figure S15a), enabling the electrostatic control of electron concentration as a function of gate voltage (V_g). The gate-voltage-dependent PL measurements were performed at an excitation power density of 0.196 kW/cm². As shown in Figures S15c and S15d, the charge neutral points of the bare WS₂ device were determined at $V_g \cong -14\text{ V}$ and $V_g \cong -9\text{ V}$ under the vacuum (Figure S15c) and air (Figure S15d) ambient conditions, respectively. We calculated the electron densities in the bare WS₂ device at the vacuum and air environments using the equation $\Delta n_{WS_2} = C \times (V_g - V_{neutral})/e$, where Δn_{WS_2} indicates the electron density injected by the gate voltage, C is the capacitance of the used *h*-BN layer ($6.55 \times 10^{-4}\text{ F}\cdot\text{cm}^{-2}$), V_g is the gate voltage, $V_{neutral}$ is the onset voltage determined by the neutral point, and e is the electronic charge.^[19] The electron densities were estimated to be $1.15 \times 10^{13}\text{ cm}^{-2}$ (vacuum) and $3.69 \times 10^{12}\text{ cm}^{-2}$ (air) at $V_g = 0\text{ V}$, respectively, while those estimated using mass-action law were $1.11 \times 10^{13}\text{ cm}^{-2}$ and $2.29 \times 10^{12}\text{ cm}^{-2}$ at the vacuum and air environments, respectively, showing a good agreement. In-between the vacuum and the air environments, the free electron density induced by the desorption of oxygen molecules is estimated to be $7.77 \times 10^{12}\text{ cm}^{-2}$ by considering the difference in the free electron densities at the vacuum and air environments. Since an oxygen molecule gains 1.083 electrons from WS₂,^[2] the number of desorbed/adsorbed oxygen molecules on the sulfur vacancies were estimated to be $7.17 \times 10^{12}\text{ cm}^{-2}$.

On the other hand, we also fabricated the *h*-BN encapsulated WS₂ capacitor devices (Figure S15b). As shown in Figures S15e and S15f, the charge neutral points of the *h*-BN encapsulated WS₂ device were determined at $V_g \cong 0.5\text{ V}$ for both the vacuum and air ambient conditions, resulting in the electron densities of $2.05 \times 10^{11}\text{ cm}^{-2}$.

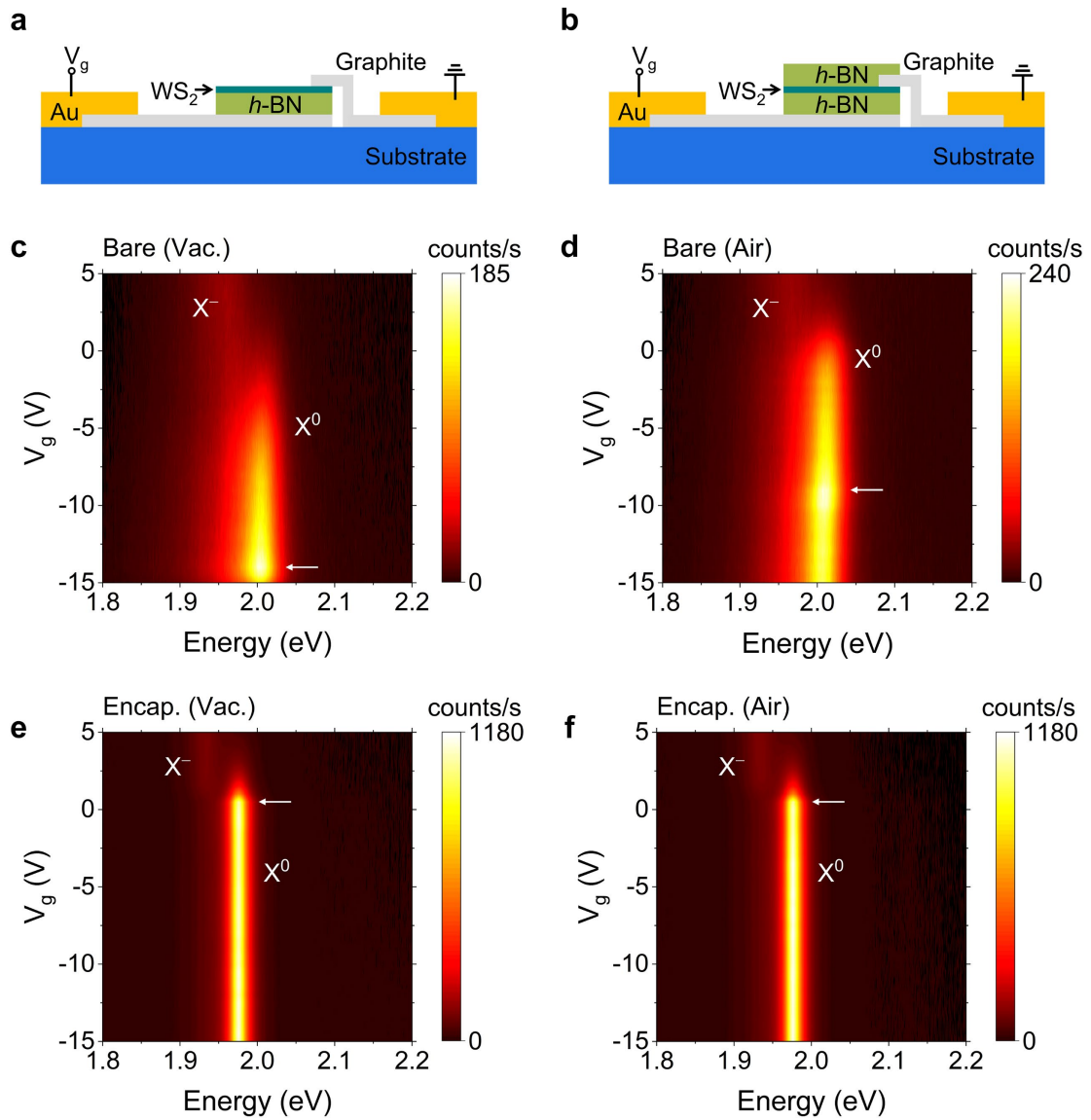


Figure S15. a,b) Schematic illustration for the bare (a) and *h*-BN encapsulated (b) WS₂ capacitor devices. c,d) Gate-voltage-dependent photoluminescence spectral maps for the bare WS₂ device under the vacuum (c) and air (d) ambient conditions. e,f) Gate-voltage-dependent photoluminescence spectral maps for the *h*-BN encapsulated WS₂ device under the vacuum (e) and air (f) ambient conditions.

S16. Photoluminescence decay curves of the neutral excitons under the vacuum ambient condition

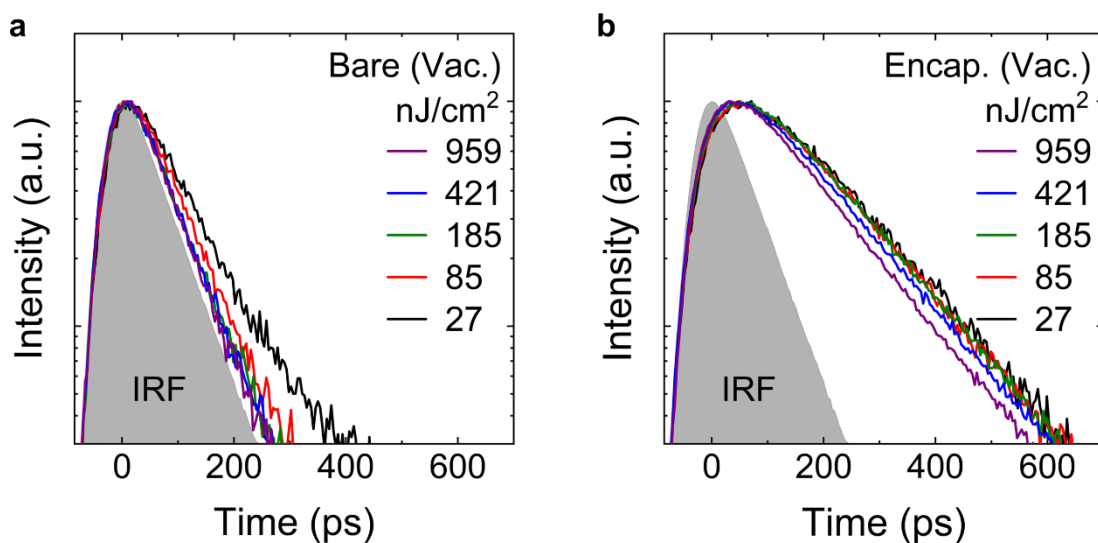


Figure S16. a,b) Photoluminescence decay curves of the neutral excitons measured as a function of the excitation power density for the bare (a) and *h*-BN encapsulated (b) WS₂ crystals under the vacuum ambient condition.

S17. Lifetime of excitons for the bare and *h*-BN encapsulated WS₂ measured as a function of the energy fluence

To extract the lifetime of excitons measured in the vacuum and air ambient conditions for the bare and *h*-BN encapsulated WS₂, the time-resolved photoluminescence decay curves are fitted using an exponential model based on instrument response function (IRF) defined as the following equation:

$$I(t) = \int_{-\infty}^t IRF(t')A_1 e^{-\frac{t-t'}{\tau_1}} dt$$

where A_1 and τ_1 are the amplitude and the lifetime for the single exciton component.

Table S1. The lifetime of the neutral excitons measured as a function of the energy fluence for the bare WS₂ under the vacuum and air ambient conditions.

Energy fluence (nJ/cm ²)	Vacuum (bare)	Air (bare)
27	49 ps	74 ps
85	37 ps	63 ps
185	33 ps	57 ps
421	27 ps	47 ps
959	19 ps	43 ps

Table S2. The lifetime of the neutral excitons measured as a function of the energy fluence for the *h*-BN encapsulated WS₂ under the vacuum and air ambient conditions.

Energy fluence (nJ/cm ²)	Vacuum (encap.)	Air (encap.)
27	139 ps	136 ps
85	136 ps	133 ps
185	132 ps	129 ps
421	126 ps	123 ps
959	116 ps	113 ps

S18. Exciton lifetime as a function of free electron density and annihilation rate constant in the *h*-BN encapsulated WS₂ capacitor devices

Table S3. The lifetime of the neutral excitons in the *h*-BN encapsulated WS₂ capacitor device measured as a function of the gate voltage at a fixed pump fluence of 27 nJ/cm².

Gate voltage (V)	Injeced electron density (cm ⁻²)	Lifetime (ps)
0.5	2.05×10^{11}	139
0.6	2.46×10^{11}	99
0.7	2.87×10^{11}	62
0.8	3.28×10^{11}	45
0.9	3.69×10^{11}	36

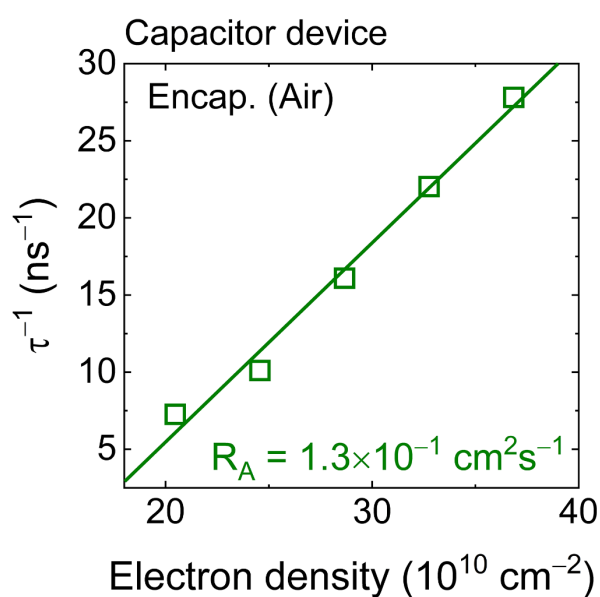


Figure S18. Recombination rate (τ^{-1}) as a function of free electron density for the *h*-BN encapsulated WS₂ capacitor devices. A linear fit for the τ^{-1} results in the exciton annihilation rate constant (R_A) due to the exciton-to-trion conversion process.

S19. Gate-voltage-dependent photoluminescence decay curves of the neutral excitons in the *h*-BN encapsulated WS₂ capacitor devices

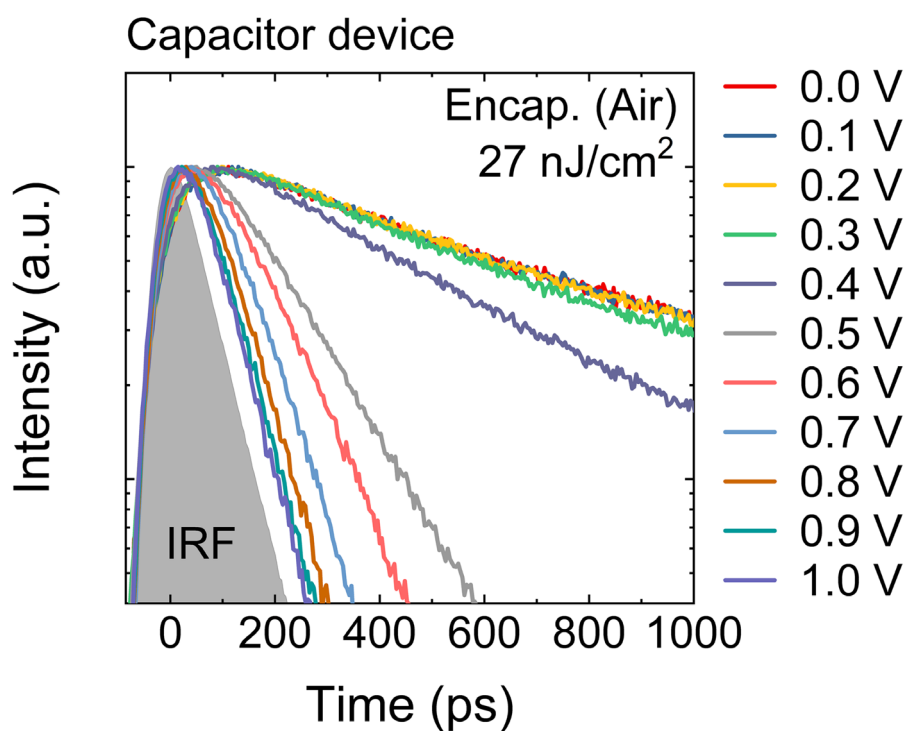


Figure S19. Gate-voltage-dependent photoluminescence decay curves of the neutral excitons in the *h*-BN encapsulated WS₂ capacitor devices under the air ambient condition.

References

- [1] H. Nan, Z. Wang, W. Wang, Z. Liang, Y. Lu, Q. Chen, D. He, P. Tan, F. Miao, X. Wang, J. Wang, Z. Ni, *ACS Nano* **2014**, *8*, 5738.
- [2] H. Liu, N. Han, J. Zhao, *RSC Adv.* **2015**, *5*, 17572.
- [3] D. Ma, B. Ma, Z. Lu, C. He, Y. Tang, Z. Lu, Z. Yang, *Phys. Chem. Chem. Phys.* **2017**, *19*, 26022.
- [4] T. Kato, T. Kaneko, *ACS Nano* **2016**, *10*, 9687.
- [5] G. Plechinger, P. Nagler, J. Kraus, N. Paradiso, C. Strunk, C. Schüller, T. Korn, *Phys. Status Solidi RPL* **2015**, *9*, 457.
- [6] A. V. Stier, N. P. Wilson, G. Clark, X. Xu, S. A. Crooker, *Nano Lett.* **2016**, *16*, 7054.
- [7] R. Senga, K. Suenaga, *Nat. Commun.* **2015**, *6*, 7943.
- [8] J. Pető, T. Ollár, P. Vancsó, Z. I. Popov, G. Z. Magda, G. Dobrik, C. Hwang, P. B. Sorokin, L. Tapasztó, *Nat. Chem.* **2018**, *10*, 1246.
- [9] Karl-Franzens-Universität Graz, ELK code, <http://elk.sourceforge.net>.
- [10] J. P. Perdew, W. Y. Wang, *Phys. Rev. B* **1992**, *45*, 13244.
- [11] G. B. Liu, W. Y. Shan, Y. Yao, W. Yao, D. Xiao, *Phys. Rev. B* **2013**, *88*, 085433.
- [12] D. H. Lien, S. Z. Uddin, M. Yeh, M. Amani, H. Kim, J. W. A. III, E. Yablonovitch, A. Javey, *Science* **2019**, *364*, 468.
- [13] T. Godde, D. Schmidt, J. Schmutzler, M. Aßmann, J. Debus, F. Withers, E. M. O. O. Del Pozo-Zamudio, V. Skrypka, K. S. Novoselov, M. Bayer, A. I. Tartakovskii, *Phys. Rev. B* **2016**, *94*, 165301.
- [14] X. X. Zhang, Y. You, S. Y. F. Zhao, T. F. Heinz, *Phys. Rev. Lett.* **2015**, *115*, 257403.
- [15] J. Siviniant, D. Scalbert, A. V. Kavokin, D. Coquillat, J. P. Lascaray, *Phys. Rev. B* **1999**, *59*, 1602.
- [16] S. Mouri, Y. Miyauchi, K. Matsuda, *Nano Lett.* **2013**, *13*, 5944.
- [17] A. Ramasubramaniam, *Phys. Rev. B* **2012**, *86*, 115409.
- [18] B. Zhu, X. Chen, X. Cui, *Sci. Rep.* **2015**, *5*, 9218.
- [19] Y. Shimazaki, I. Schwartz, K. Watanabe, T. Taniguchi, M. Kroner, A. Imamoğlu, *Nature* **2020**, *580*, 472.